International Journal of Rock Mechanics & Mining Sciences 174 (2024) 105640

Contents lists available at ScienceDirect

International Journal of Rock Mechanics and Mining Sciences

journal homepage: www.elsevier.com/locate/ijrmms

A novel graph-based 3D breakage method for angular particles with an image-based DEM

Mehryar Amir Hosseini , Pejman Tahmasebi *

Colorado School of Mines, Golden, CO 80401, USA

A R T I C L E I N F O

Keywords:
Particle breakage
Discrete element method (DEM)
3D breakage model
Fracture surfaces

A B S T R A C T

Particle breakage has been investigated extensively in a variety of applications. The Discrete Element Method (DEM) is commonly used to investigate breakage. However, it has limitations in accurately representing the natural morphology of particles. Additionally, existing techniques for simulating breakage of irregular particles have mainly focused on splitting and chipping mechanisms, simplifying fractures as straight lines or flat planes. In this paper, we introduce a novel 3D breakage model that incorporates all breakage mechanisms (splitting, chipping, and fragmentation). To determine fracture surfaces, we apply Dijkstra's algorithm to the particle's stress field to find the fracture surface(s). After defining the fracture surface(s), the intersection set operations and 26 connected components labeling techniques are employed to generate multiple sub-grains. We apply our method to a compression test on a three-particle system to demonstrate its effectiveness in modeling breakage. We conduct quantitative analyses on grain count, mass, displacement, kinetic energy, rotational motions, and inter-particle forces. Our findings indicate that particle displacement is a significant factor in breakage, while the influence of rotational motion should not be overlooked. Furthermore, our results capture different phases of breakage and rotational movements.

1. Introduction

Particle breakage (i.e., fracture) can be seen in a wide range of applications, and the behavior of the broken particles has been known as an effective parameter in many industries and engineering applications related to solid and rock mechanics,[1] geotechnical,[2] pharmaceutical,[3,4] ocean engineering,[5] lithotripsy,[6] etc. Particle breakage has been identified as a micro-scale behavior of granular assembly, although it can change the macro-scale behavior of such systems.[7] The breakage of a particle produces sub-particles with different geometrical characteristics (i.e., shape), leading to their different behavior from the original particle. To be more specific, at the microscale, the redistribution of stress within sub-particles resulting from breakage alters the inter-particle dynamics of the system. Additionally, when a broken particle is in contact with unbroken and/or broken grains, it becomes crucial to comprehend the inter-particle interactions and their behaviors. Breakage can occur in a particle when the applied stress reaches its yielding strength. The magnitude and location of the applied stress can influence the likelihood of breakage, the path of fracture, and the type of breakage.

The breakage phenomenon can be classified into three distinct forms: (*i*) chipping, characterized by the generation of sub-particles with significant differences in size; (*ii*) splitting, where a particle breaks into two nearly equal-sized sub-particles; and (*iii*) fragmentation, where a particle shatters into multiple pieces. Each of these scenarios plays a significant role in the breakage process. While chipping and splitting cases have received considerable attention, the fragmentation mechanism remains poorly understood due to the intricate nature of fracture surfaces under such conditions. Moreover, previous studies[8–11] have emphasized the importance of considering the particle's shape during the breakage process, as it influences key grain parameters such as positioning, interlocking, and fracture characteristics.

In experimental studies, capturing the microscale behaviors of breakage can be costly and challenging. As an alternative, numerical methods offer a way to investigate the behavior of broken and unbroken particles in such systems. Among the numerical methods, the Discrete Element Method (DEM) proposed by Cundall and Strack,[12] has been widely adopted by researchers studying breakage. In the literature, sphere-based methods are commonly used to simulate particle breakage with DEM. One approach involves creating a grain using sub-spheres

* Corresponding author.
E-mail address: tahmasebi@mines.edu (P. Tahmasebi).

https://doi.org/10.1016/j.ijrmms.2024.105640
Received 7 July 2023; Received in revised form 13 December 2023; Accepted 3 January 2024

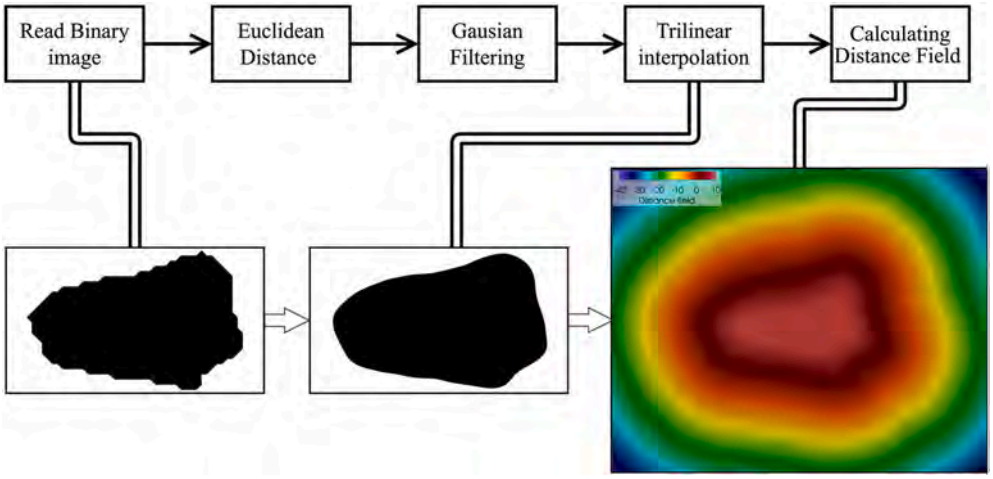

Fig. 1. The implemented image analysis technique to capture the morphology of a particle from XRCT and apply the Gaussian filtering and trilinear interpolation to eliminate pixelated areas.

that are bonded together. The parallel bond model (BPM)[13–17,19] and the flat-joint model (FJM)[18,13,20,21]) have been extensively used to bond the sub-spheres. These models allow for the creation of non-spherical particles by increasing the number of sub-particles. However, this approach significantly increases the computational cost, and even with a large number of sub-spheres, it is unable to accurately represent the natural shape of a particle with complex concavities, convexities, and sharp features. This issue is discussed and tested elsewhere.[22] Furthermore, a previous study[23] demonstrated that the breakage behavior is influenced by the number of sub-spheres and bonding parameters.

The replacing approach is another sub-sphere technique to model breaking particles.[24–28] In this method, when a particle reaches its failure strength, it is substituted with smaller spheres. However, determining the properties of these smaller spheres, such as their diameter and mass, in relation to the original grain can be complex and may not accurately reflect reality. While the computational cost of this replacement approach is lower compared to the sub-sphere method, it is unable to capture the natural shape of the particles.

The Bonded Block Model (BBM) is another technique used for modeling breakage. In the BBM, the sub-spheres used in sphere-based approaches are replaced by rigid polyhedral elements that are bonded together to form a grain. Similar to sphere-based methods, the results of the BBM are influenced by the bonding parameters. However, the BBM method is unable to capture the concavity of a particle's natural morphology. Another technique that can closely represent the shape of natural particles is the Finite-Discrete Element Method (FDEM). However, the effectiveness of the FDEM is highly dependent on the number of meshes (faces) used to create the particles, and the method is associated with high computational costs.

To capture the morphology of particles when undergoing breakage, advanced DEM methods (e.g., Level Set-DEM) has also been used.[29,30] In this approach, X-ray computed tomographic (XRCT) images are used[31] to capture the natural shape of a grain. A mathematical function should be defined to read the XRCT images in the computational code. To do so, the Potential Particle Method (PPM)[32] can interpret the binary images from XRCT in the code. The PPM defines the aforementioned mathematical function (Π) to categorize the coordinates into: (i) inside ($\Pi > 0$), (ii) outside ($\Pi < 0$), and (iii) on surface ($\Pi = 0$). Within a similar line of accurate DEM modeling, Zhang and Tahmasebi also proposed a multiphysics framework with much less computational burden using Enhanced Distance Transform (EDT).[33] The former approach was also resigned to deal with fracturing, and it only takes into account the splitting breakage mechanism and does not consider the fragmentation scenario.[29,30] Furthermore, this approach suggests creating a fracture path by connecting points with the highest force, resulting in a flat fracture plane. Treating the fracture as a flat plane can be unrealistic, although it simplifies the breakage process and its calculations. Moreover, in a 3D system, a particle in contact with two other grains cannot break, even if it meets the breakage criteria, because, in a 3D system, at least three contact forces are required to form a fracture plane. To incorporate the fragmentation scenario in breakage, another study utilized stress field calculations in their investigation of 2D polygonal shapes to determine the fracture path(s).[34] While using the stress field in grains can provide valuable insights for modeling fragmentation during breakage, their assumption of the particle as a polygon and the consideration of fracture path(s) as lines may not achieve the desired accuracy.

Up to this point, the limitations of previous methods in capturing the natural shape of grains, neglecting fragmentation, and assuming a flat fracture plane have been emphasized. Therefore, there is a need to develop a systematic breakage algorithm to address these research gaps in the field. In this regard, we have employed the iDEM (image-based Discrete Element Method), which has demonstrated its capabilities in accurately modeling irregular particles.[22,33,35]

The remaining sections of this paper are structured as follows. Section 2 will delve into the governing equation of the iDEM, the methodology for finding fracture path(s), and the breakage algorithm. In Section 3, the results of the study will be presented, illustrated, and discussed. Finally, Section 4 will provide the conclusion and summary of the investigation.

2. Numerical method

In this section, we will provide a detailed explanation of the developed numerical method. Firstly, we will elaborate on the image-based Discrete Element Method (iDEM), which enables us to accurately capture the natural morphology of grains, determine in-contact particles, calculate properties of irregular particles, and simulate the motion of grains. Following that, we will discuss the proposed breakage process and its characteristics. This includes the breakage criteria used, the calculations of post-breakage properties, and the algorithm of the model.

2.1. Image-based Discrete Element Method (iDEM)

As mentioned earlier, the natural morphology of a particle can be accurately captured using image analysis techniques. In this regard, we will discuss the Enhanced Distance Transform method (EDT) that we have employed to capture the morphology of particles and also converting the binary images into useful contours for penetration

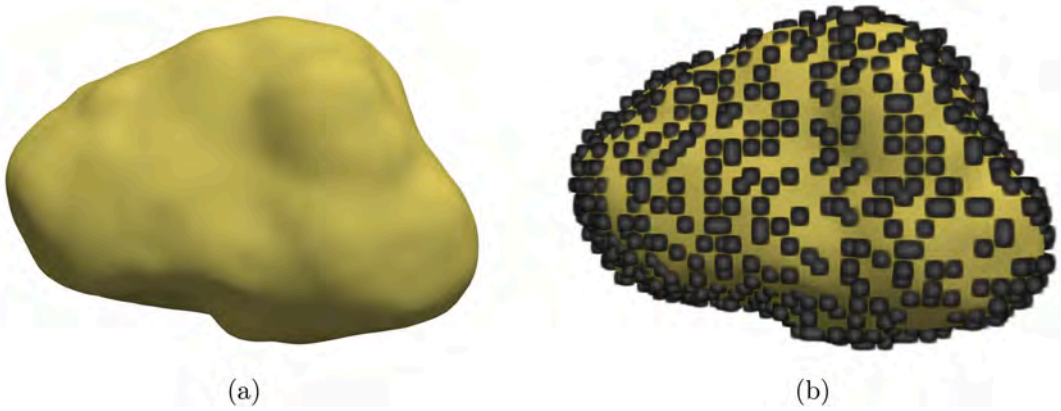

Fig. 2. Demonstration of (a) the 3D natural shape of the particle and (b) the nodes on the surface of the irregular particle ($D^p = 0$) to deploy the node-to-surface method.

calculations. Moreover, we will delve into the calculation of characteristic properties, such as particle mass, based on the captured morphology. To calculate the inter-particle forces, we first need to determine if a collision occurs between a particle and other particles or walls. We will elaborate on the contact detection process, which involves identifying and analyzing the collisions between particles. Once the contacts are detected, we can proceed to calculate the forces between particles (particle-particle forces) as well as between particles and walls (particle-wall forces). These forces will then be applied to the grains to determine the motion of each particle.

2.1.1. *Image analysis technique*

To capture the real morphology of a particle, we need to use the binary images produced using XRCT to construct a particle. Each binary image consists of pixels inside (i), outside (o), and boundary (b) of a grain. The first step of image analysis is to measure the distance between the inside and those on the boundary of the particles (d^{i-b}). Some methods can be used to calculate the minimum of d^{i-b}, including chessboard, city block, and Euclidean. In our approach, we employ the widely-used Euclidean method. Using the Euclidean method, the minimum distance d^{i-o}_{min} can be calculated.[36] The Euclidean distance method generates a field where outside points are assigned negative values while the inside point receives a positive value. However, the calculation of the distance field on the image's pixels can result in pixelation and loss of smoothness in the images. To address this issue, we enhance our proposed method by incorporating Gaussian filtering and trilinear interpolation.[37] Gaussian filtering is applied to the entire domain, while trilinear interpolation is specifically used on the pixels near the surface. This helps to eliminate sharp transitions in those areas and improve the resolution of the distance value at coordinate p (D^p), using the trilinear interpolation. Additionally, trilinear interpolation is employed during contact detection and overlap calculations to enhance the accuracy of these steps. The discussed steps to capture the natural morphology of grain are summarized in Fig. 1.

The properties of each particle should be calculated based on the calculated EDT 3D map. To this end, the mass of grain, the center of mass, and the moment of inertia are calculated based on previous studies on the iDEM. These equations can be found elsewhere.[22,33,35,37]

2.1.2. *Finding in-contact particles*

In the conventional Discrete Element Method, the initial step involves identifying the particles that are in contact in order to calculate inter-particle and particle-wall forces. However, determining these values can be complex when dealing with non-spherical particles like the ones in our study. To address this challenge, we employ the node-to-surface method. Since the distance field values for the particle surfaces are close to zero, we strategically place nodes at coordinates where $D^p \cong 0$. By using the node-to-surface technique, contact detection and overlap calculations can be performed for these irregular particles. Fig. 2 showcases a 3D particle and the results obtained using the node-to-

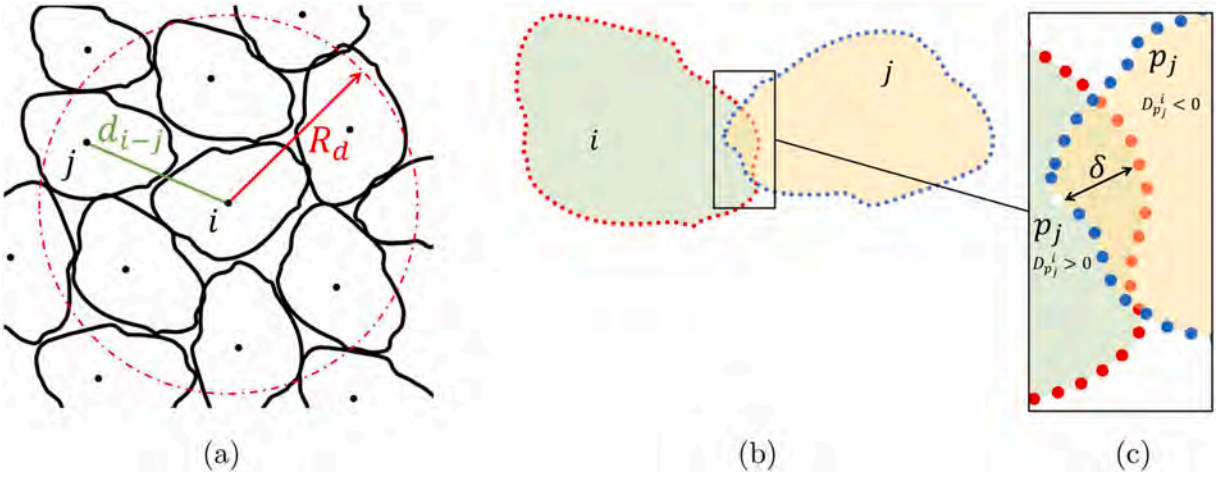

Fig. 3. (a) Initial in-contact guess based on the detection radius to decrease computational cost. (b) Two irregular particle in-contact (c) overlap checking procedure to check the presence of overlap between these particles and measure the overlap value to calculate inter-particle forces. Note: the overlap is exaggerated for illustration purposes.

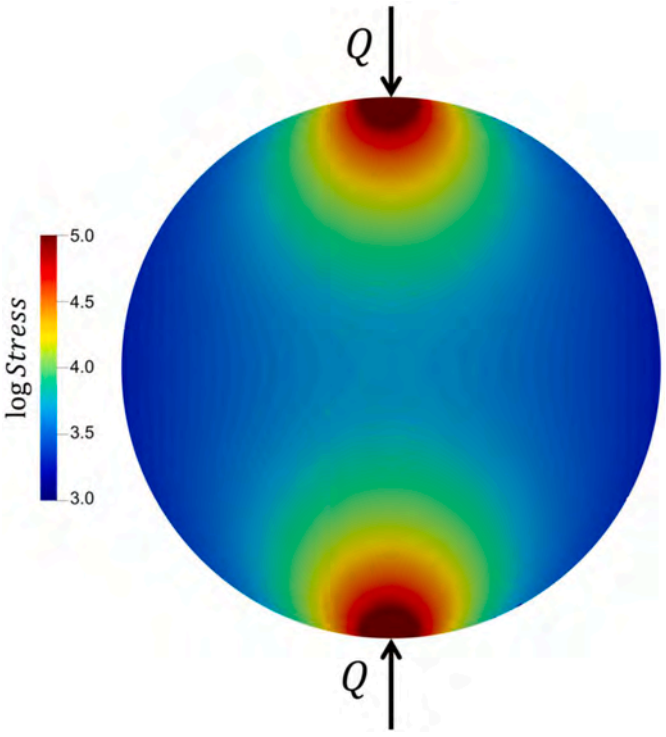

Fig. 4. Stress calculation for a spherical particle based on the Boussinesq equation.

surface method.

Once nodes are assigned on the surface of irregular particles, we need to establish a procedure to identify and measure the overlap between these particles. This procedure will be explained specifically for particle-particle contacts, but it can also be applied to interactions between particles and walls. To detect contact, we compare the coordinates of nodes on one particle with the distance fields of other particles. In other words, we check if the coordinates of a node on particle j (p_j) fall within the distance field of particle i ($D_{p_j}^{i}$). To enhance the accuracy of overlap estimation, we employ trilinear interpolation when calculating $D_{p_j}^{i}$, the trilinear interpolation is also implemented to increase the accuracy of overlap estimation. If $D_{p_j}^{i} < 0$, then particles i and j are in-contact in node p_j. To reduce the computational burden, we initially guess the potential in-contact particles for each particle. This is achieved by defining a detection radius (R_d) around particle i within which we search for particles that could potentially come into contact with particle i. Qualified grains (i.e., $|d_{i-j}| \leq |R_d|$, where d_{i-j} is the distance between particle i and j center of mass) should be checked for the existence of overlap with the procedure as mentioned earlier. The applied procedure to solve the complexity of contact detection can be found in Fig. 3. The overlap between in-contact particles (δ) can be calculated as the difference between the distance fields of each in-contact grain. The procedure for calculating the overlap between particles and particle-wall can be found elsewhere.[33,35,37] The interparticle force direction can also be measured using the contact normal vector ($\overrightarrow{C_{ij}^{n}}$) expressed as:

$$\overrightarrow{C_{ij}^{n}} = -\frac{\nabla D_{p_j}^{i}}{\left\|\nabla D_{p_j}^{i}\right\|}. \tag{1}$$

2.1.3. Particle motion governing equations

This section focuses on the governing equations derived from the Discrete Element Method (DEM). The DEM is capable of determining the behavior of individual particles within the computational domain. The motion of a particle can be classified into rotational and translational motions. By applying Newton's Second Law, the DEM calculates these motions and the trajectory of the particle. Therefore, the motions can be computed using the following equations:

$$m_i \frac{dV_i}{dt} = \sum_j F_{ij}^{pp} + \sum_j F_i^{wp} + F_i^{ext}, \tag{2}$$

$$\frac{d\omega_i}{dt} I_i = \sum_j M_{ij} + \sum_j M_w, \tag{3}$$

where m_i is the mass of particle i (Eq. (2)), and the velocity of particle i is defined as V_i. F_{ij}^{pp} and F_i^{wp} are the inter-particles and particle-wall forces, respectively. F_i^{ext} is the external forces that can be applied to particle i, which in this work the external force is gravity. Moreover, ω_i is the rotational velocity and I_i is particle i's moment of inertia in Eq. (3). The inter-particles and wall-particle torques are also presented as M_{ij} and M_w. F_{ij}^{pp} is:

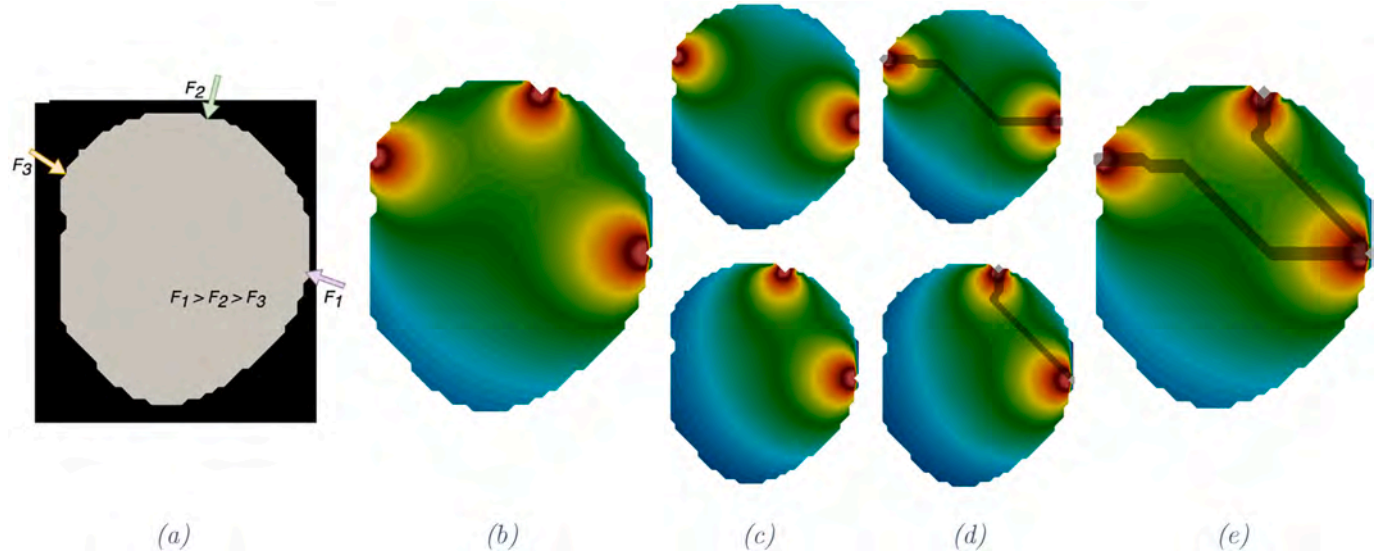

Fig. 5. 2D visualization of (a) Main particle and applied forces, (b) calculated stress field, (c) stress field for coupled forces, (d) calculated fracture path (black) for each coupled force, and (e) combination of coupled forces and fracture paths.

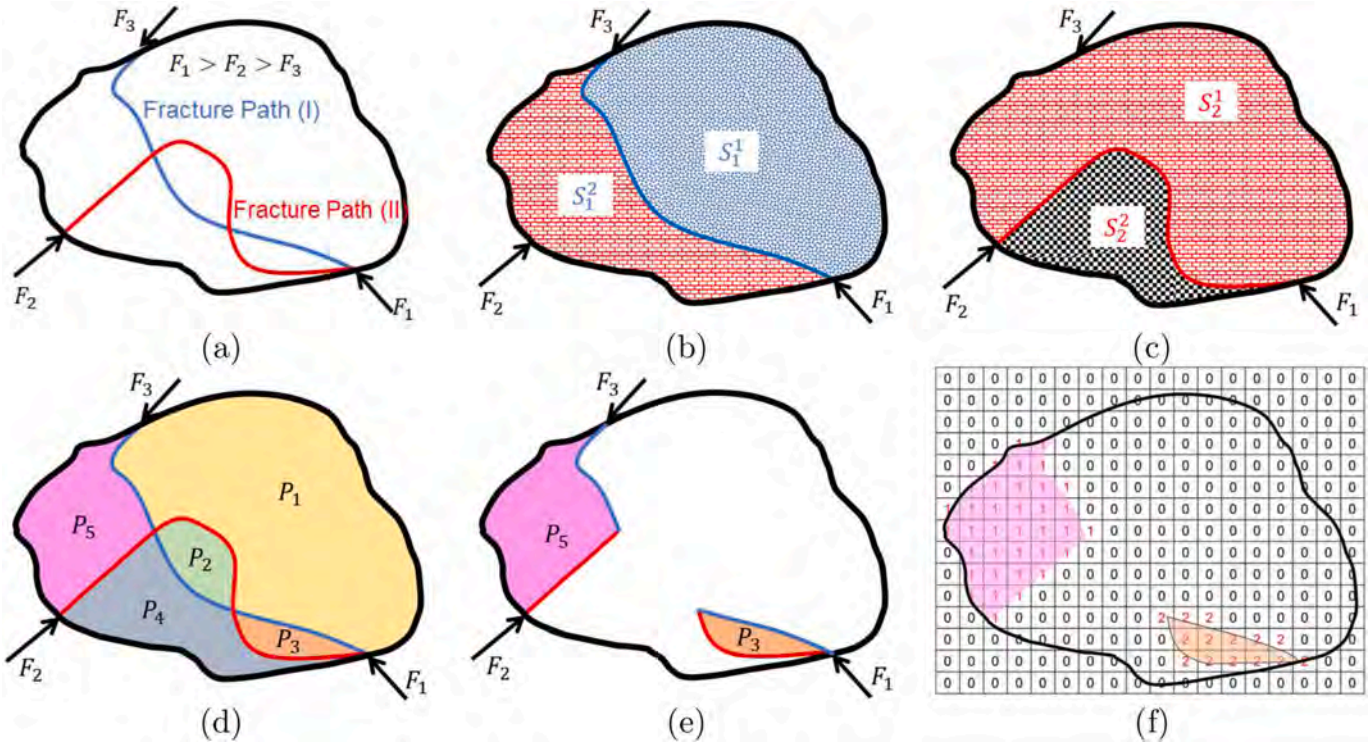

Fig. 6. 2D presentation of (a) Sample particle and calculated paths where have intersections, (b) calculated sub-sections for the fracture path (I), (c) calculated sub-sections for the fracture path (II), (d) sub-grains, (e) sub-grains which set operations cannot separate, and (f) label field to separate those sub-grains with 26 connected-component labeling technique.

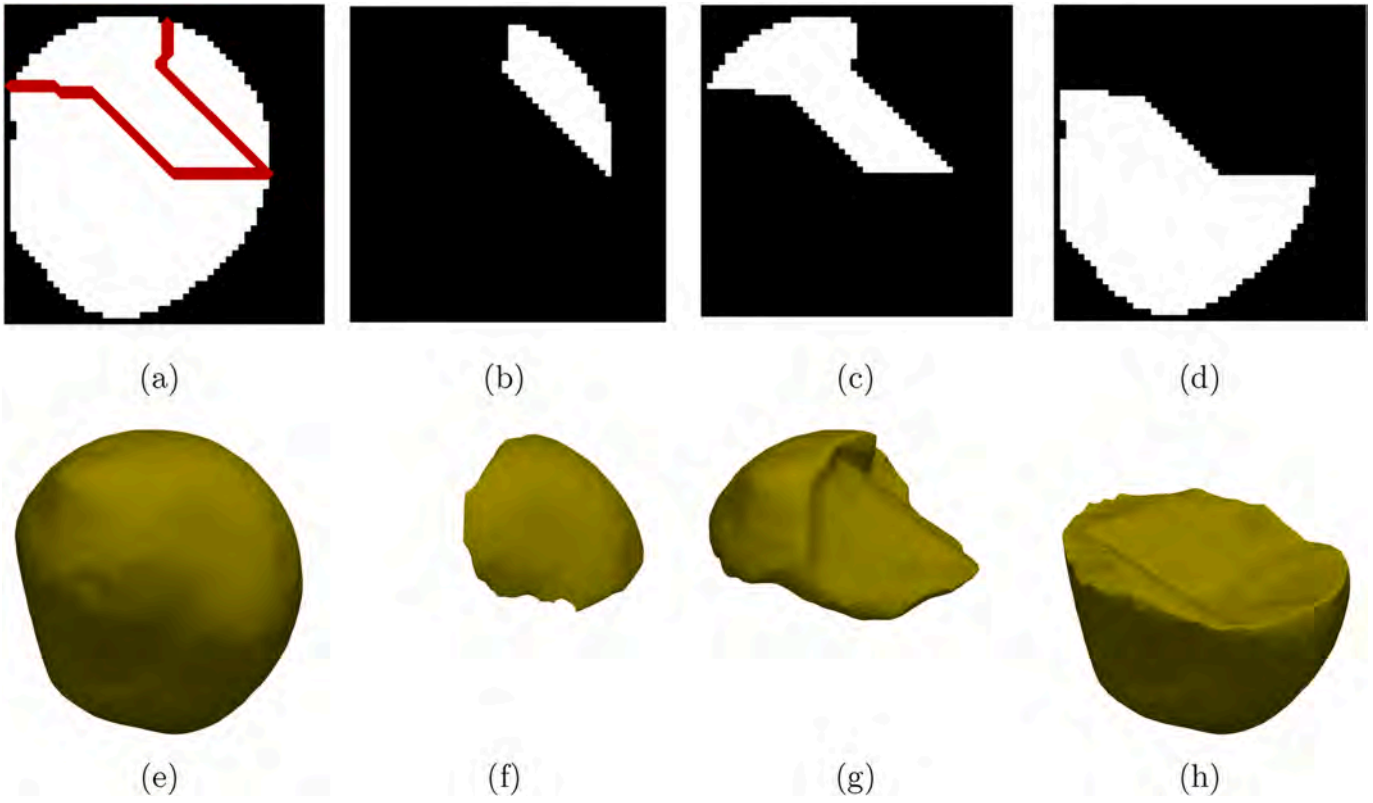

Fig. 7. 2D illustration of (a) Main particle and fracture paths, (b), (c), and (d) are fragments created by this breakage scenario and 3D demonstration of (e) main particle. (f), (g), and (h) are post-breakage sub-grains resulting in breakage.

Table 1
Properties of particles used in the simulations.

Property	Value
Normal stiffness (N/m)	7×10^6
Shear stiffness (N/m)	7×10^6
Friction Coefficient	0.4
Weibull's modulus	3
Time step (s)	1×10^{-9}
Breakage Criteria (MPa)	100
Density (kg/m^3)	2650
Diameter (mm)	0.75

$$F_{ij}^{pp} = \sum_{n=1}^{N} \left(F_{ij}{}^{norm}\right)_n + \sum_{n=1}^{N} \left(F_{ij}{}^{tan}\right)_n, \tag{4}$$

where N is the number of nodes on particle i that are inside particle j. Also, F_{ij}^{norm} and F_{ij}^{tan} are the normal and tangential contact forces, respectively, expressed as:

$$F_{ij}{}^{norm} = -K\delta_{ij}C_{ij}^{n}, \tag{5}$$

$$F_{ij}{}^{tan} = R\left(F_{ij}{}^{tan}\right)_{t+dt} - \alpha K\left[V_{ij} - \left(V_{ij}.C_{ij}^{n}\right)C_{ij}^{n}\right]dt, \tag{6}$$

where K is the normal stiffness, the rotational matrix is R, dt is time-step, α is the normal and shear stiffness ratio, and relative velocity (V_{ij}) also expressed as:

$$V_{ij} = V_i + \omega_i \times \left(\vec{P}_c - \vec{c}_i\right) - V_j - \omega_j \times \left(\vec{P}_c - \vec{c}_j\right), \tag{7}$$

where $\vec{c}_i$ and $\vec{c}_j$ are particle's i and j center of mass, respectively. Also, $\vec{P}_c$ is the position of the contact point. The inter-particle moments (M_{ij} and M_{ji}) for overlapped grains can be formed as:

$$M_{ij} = F_{ij}^{pp}\left(\vec{P}_c - \vec{c}_i\right), \tag{8}$$

$$M_{ij} = F_{ji}^{pp}\left(\vec{P}_c - \vec{c}_j\right). \tag{9}$$

The calculated contact force for particle i is applied on particle j by action-reaction rule ($F_{ij}^{p} = -F_{ji}^{p}$)

2.2. Breakage model

To this point, we have described the iDEM approach using which one can capture the natural shape of particles and incorporate the governing equations of the DEM to calculate applied forces and particle motions. As mentioned, in order to address the discussed research gap on fracturing, it is necessary to develop an algorithm that can encompass the scenarios of chipping, splitting, and fragmentation in 3D breakage. The proposed breakage procedure aims to systematically address two fundamental questions: (*i*) when a particle should break and (*ii*) how it breaks. The first question can be answered by comparing the calculated stresses on a particle with the breakage criteria. However, to answer the second question, techniques need to be deployed to handle the complexity of calculating multiple fracture paths and to avoid using flat and unrealistic planes as fracture surfaces.

2.2.1. Breakage detection

In this section, we will discuss the procedure designed to detect the occurrence of breakage. Breakage can occur when a grain is in contact with other particles or walls. Therefore, the computational domain needs to be searched to identify particles that are in contact with other grains or walls. Additionally, for breakage to occur, the applied stress on a particle (σ_i) must reach the breakage criteria. The stress applied on each particle can be calculated as follows[38]:

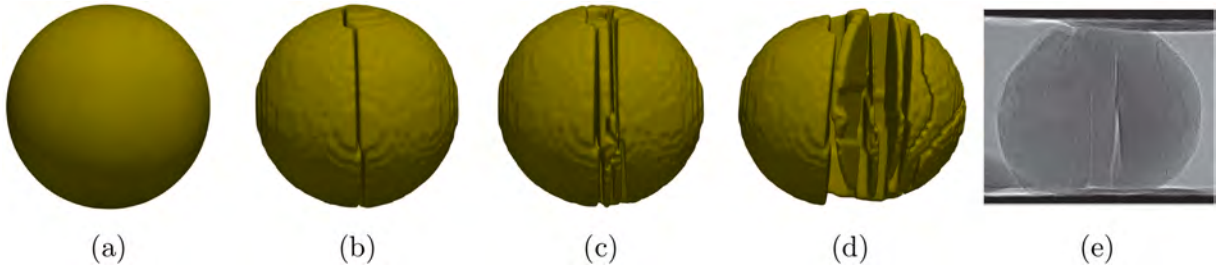

Fig. 8. Demonstration of a spherical particle under 1-D compression at time-step (a) 0, (b) 7,000, (c) 14,000, (d) 18,000. (e) Experimental data from Cil and Alshibli.[23]

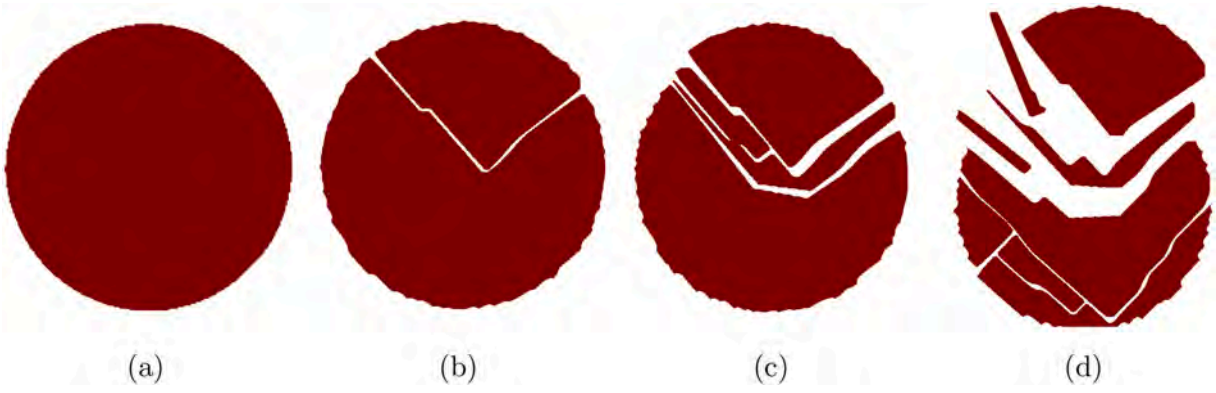

Fig. 9. 2D top-view of a spherical particle under 1-D compression at time-step (a) 0, (b) 7,000, (c) 14,000, (d) 18,000.

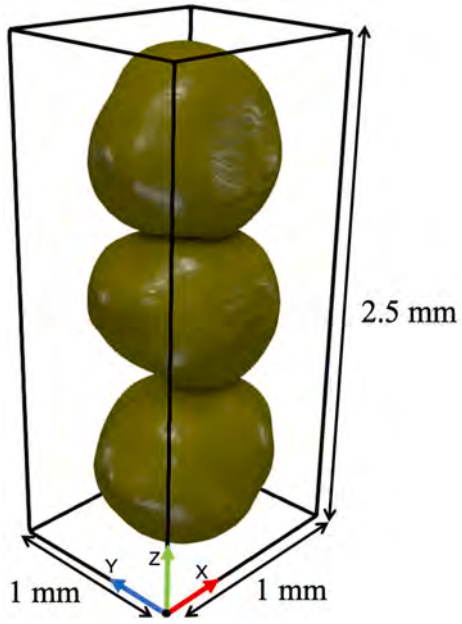

Fig. 10. 3D Demonstration of the domain and grains in the modeled three-particle breakage system.

$$\sigma_i = \frac{\rho}{m}\sum_{n=1}^{N}\left(\left(F_{ij}^{pp} + F_i^{pw}\right)_n \otimes \left(\overrightarrow{p}_i - \overrightarrow{c}_i\right)\right). \tag{10}$$

Then, the principal stresses (σ_i^p) are calculated as the eigenvalues of σ_i. These principal stresses can then be compared with the yielding stress criteria. In this study, the particle's stress is compared using both the Tresca and von Mises yielding criteria. In our calculations, both tensile and compressive stresses can lead to breakage. The Tresca stress (σ_T) can be defined as:

$$\sigma_T = \frac{1}{2}\max(|\sigma_1 - \sigma_2|, |\sigma_2 - \sigma_3|, |\sigma_1 - \sigma_3|), \tag{11}$$

where σ_1, σ_2, and σ_3 are principal stresses of the particle. The von Mises yielding criteria (σ_v) is presented as follows:

$$\sigma_v = \sqrt{\frac{1}{2}\left[(\sigma_1 - \sigma_2)^2 + (\sigma_1 - \sigma_3)^2 + (\sigma_3 - \sigma_2)^2\right]}, \tag{12}$$

whenever the particle's σ_v and σ_T exceeds the designated breakage stress (σ_B), then the particle can break.

2.2.2. *Finding breakage Surface(s)*

If a particle meets the breakage criteria, it is necessary to determine the breakage surface(s). In order to break the original 3D particle into sub-particle(s), the path where breakage can occur needs to be identified. It is preferable to determine the path during simulations rather than relying on user input, as a self-made breakage path can lead to conflicts in the simulation. Additionally, using an arbitrary 3D fracture path is not desirable in breakage systems, as experimental investigations would be required to accurately capture such a path. Therefore, we have developed a systematic approach to create 3D breakage paths that consider all breakage scenarios.

Among the different breakage mechanisms, fragmentation is the most complex one, as it involves multiple paths and the generation of multiple sub-particles. To address this complexity, calculating the stress field within the grain can be useful. Numerical studies have been conducted to calculate the internal stress distribution in a grain.[34,39,40] Although one can use more sophisticated approaches for defining the stress distribution within the particles, in this study the Boussinesq equation is employed, which has been validated with photoelastic experiments.[40] This approach provides a rapid and simple evaluation of stress as a scaler property.[41–43] The combination of these individual stress distributions yields the final stress field.[40] Therefore, we have implemented the Boussinesq equation to calculate the stress field in each grain as follows:

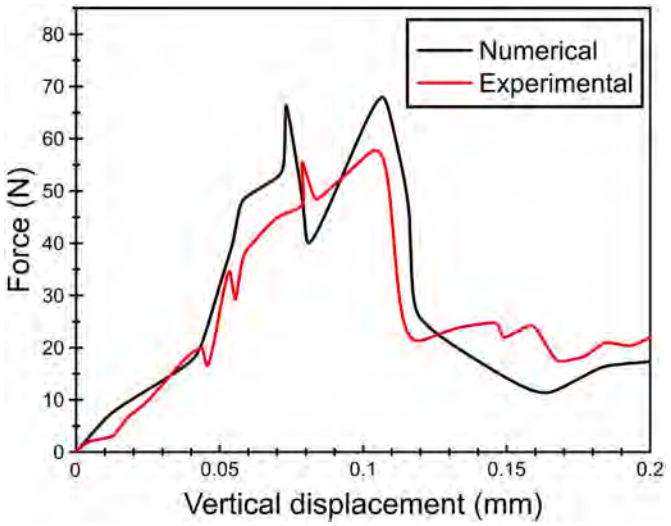

Fig. 11. Comparison between the previous experimental investigation[23] and our proposed numerical method with respect to wall force versus top wall vertical displacement.

$$\sigma_r = \frac{3Q\cos\theta}{2\pi r^2}, \tag{13}$$

where Q is the point load, r is the distance between load and point, and θ is the angle between the r and load direction; see Fig. 4.

Experimental results have shown that the fracture surface is often more likely to connect the locations of contact forces on each grain.[23,44] Taking this into account, we can utilize the node-to-surface approach in the iDEM to identify the contact forces on each particle. By determining the contact forces and their respective locations, we can then pair the highest contact force with another applied contact force on a grain, based on previous investigation on fragmentation.[34] This allows us to define the starting and ending points of the fracture path(s).

Fracture propagation is typically observed in areas of high stress, making the calculated stress field crucial for determining the fracture path. To achieve this, it is necessary to explore all potential fracture paths between two coupled forces (i.e., contact forces) and identify the path that traverses the highest stress regions in the field. In essence, we aim to find a path with the greatest cost (representing stress) between the starting and ending points. To accomplish this, we can employ the concept of Dijkstra's algorithm from graph theory.[45–47] Dijkstra's algorithm determines the minimum cost path between two points in a weighted graph among all possible paths. However, in our case, we seek a path that traverses voxels with the highest stress values. To reconcile the contradiction between the stress field and Dijkstra's algorithm, we invert the stress field, thereby prioritizing the fracture path through high-stress regions. After post-processing, including this inversion, the starting and ending points of the path (corresponding to the locations of the contact forces) are used. Consequently, Dijkstra's algorithm calculates the fracture path(s). To facilitate visualization and better understanding, we have demonstrated the step-by-step breakage process in 2D in Fig. 5. Moreover, to create smooth 3D fracture surface(s), we used the 3D minimum error cut concept[48] on the produced stress volume $\mathbb{S}$. Here, the cumulative minimum stress along the start-end direction is calculated. This algorithm starts with the first layer (k) of $\mathbb{S}$ and each voxel on this layer is denoted by $[i.j], i = 1....,p; j = 1,...,q$. Then, the cumulative minimum stress $\boldsymbol{E}$ using the closest 9 voxels is calculated on the

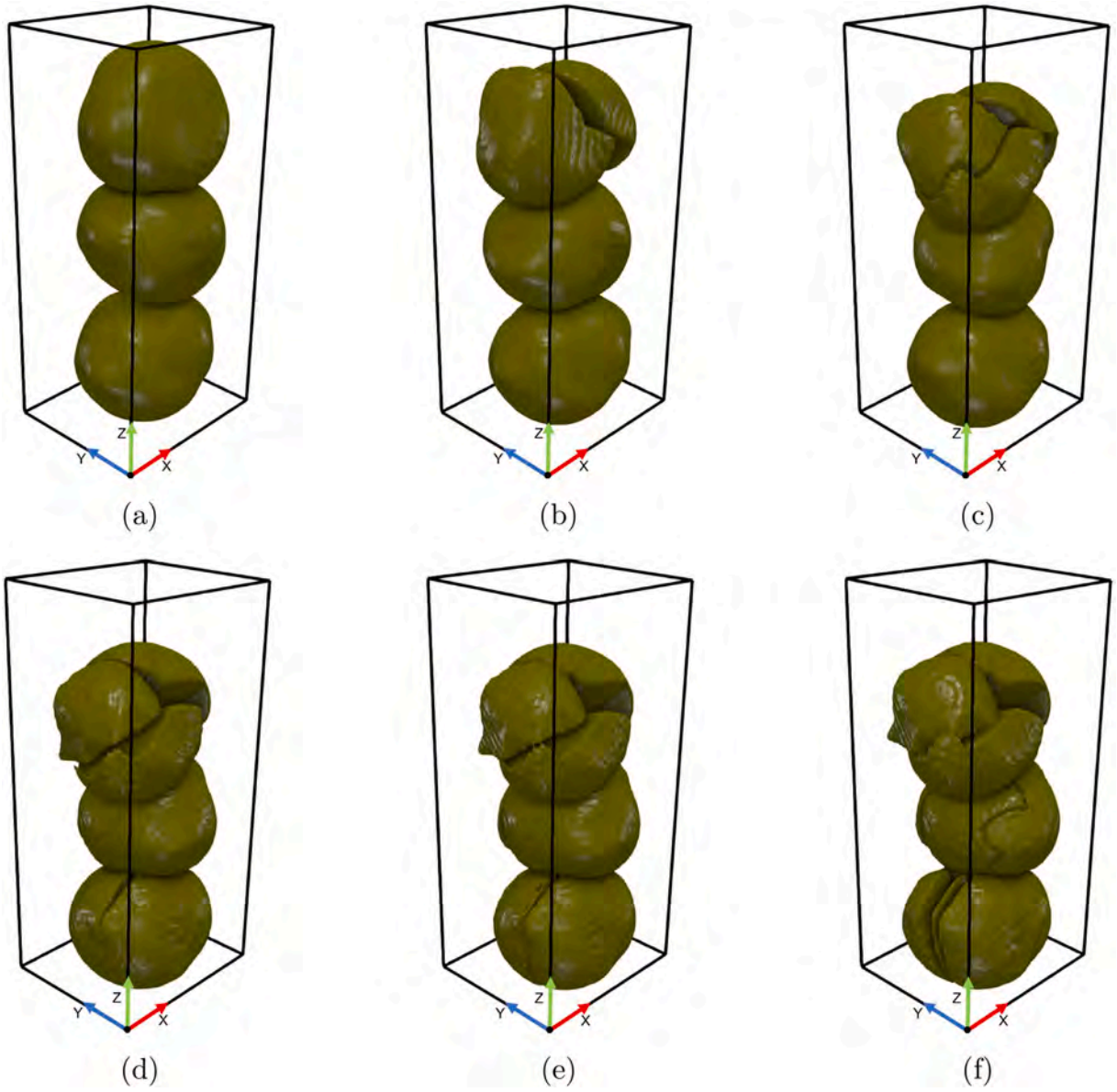

Fig. 12. Dynamic evolution of breakage process in 3D at time step (a) 0, (b) 100,000 (c) 170,000 (d) 199,000 (e) 200,000, and (f) 202,000.

previous $k-1$ layer by:

$$\boldsymbol{E}_{\mathrm{i,j,k}} = \mathbb{S}_{i,j,k} + \min\left(\begin{matrix}\boldsymbol{E}_{(\mathrm{i-1,j-1,k-1})}, \boldsymbol{E}_{(\mathrm{i-1,j,k-1})}, \boldsymbol{E}_{(\mathrm{i-1,j+1,k-1})}, \boldsymbol{E}_{(\mathrm{i,j-1,k-1})}, \boldsymbol{E}_{(i,j,k-1)}, \boldsymbol{E}_{(\mathrm{i,j+1,k-1})}, \\ \boldsymbol{E}_{(\mathrm{i+1,j-1,k-1})}, \boldsymbol{E}_{(\mathrm{i+1,j,k-1})}, \boldsymbol{E}_{(\mathrm{i+1,j+1,k-1})}\end{matrix}\right). \tag{14}$$

After defining the fracture surface, one can use the set operations (e.g., intersection) to decided how to split the original particle.[34] However, in scenarios where fracture surfaces have intersection(s), the set operations cannot split them accurately, and multiple separate fragments might be considered as a grain. To illustrate the complexity when fracture surfaces intersect each other, Fig. 6 is demonstrated in 2D. In Fig. 6(a), three forces are applied to the sample grain, and two paths are calculated based on the previously mentioned steps. Then, each path divides the original grain into two sub-sections; see Fig. 6(b) and (c). Based on paths in Fig. 6(a), five sub-grains should be produced after this breakage incident. However, set operations can only capture these:

$$\begin{cases} S_1^1 \cap S_2^1 = P_1 \\ S_1^1 \cap S_2^2 = P_2 \\ S_1^2 \cap S_2^1 = P_3 + P_5 \\ S_1^2 \cap S_2^2 = P_4 \end{cases} \tag{15}$$

where S_1^1 and S_1^2 are subdivisions which created by fracture path (I). S_2^1 and S_2^2 are subdivisions which constructed by fracture path (II). Moreover, P_1, P_2, P_3, P_4, and P_5 are sub-particles produced by fracture paths

(I) and (II). As calculated in Eq. (15), the intersection operation ($\cap$) cannot systematically separate the sub-grains P_3 and P_5, and problem can rise in creating new sub-grains; see Fig. 6(c). To tackle the issue, the 26 connected-component labeling technique has been implemented in our proposed method. The 26 connected-component labeling ensures that only one fragment exists within each sub-grain by checking the connected pixels. If multiple connected objects are detected, they will be separated, and assign each object to a separate sub-grain; see Fig. 6(f).

After fragments are created, distance fields can be generated for the new sub-grains. The 2D and 3D visualization of the main grain and fragments after the breakage process is depicted in Fig. 7. These demonstrations indicate that our proposed method can conduct fragmentation while irregular and realistic fracture surfaces are produced.

2.2.3. Calculating characteristics of new sub-particles

So far, the sub-particles and their distance field have been generated. To designate the properties to new sub-grains, we took the following steps.

1. Nodes should be allocated on the surface of each sub-particles by deploying node-to-surface method.
2. General properties of each sub-particle, including mass, center of mass, and moment of inertia, should be calculated.
3. Moreover, the material characteristics (i.e., density) of sub-particles should be allocated to them based on the original particle.
4. To minimize the computational errors, the velocity and forces of the original particle are designated to sub-particles.
5. Since we are working on the local coordinates in the broken particle, the transition from the local to the global framework should be considered to put new grains in the original particle's exact location.
6. When particles become smaller, they tend to become stronger. In light of this observation, previous studies[29,49] have proposed the following equation to account for the breakage criteria of a sub-grain after each fracture event:

$$\frac{(\sigma_B)_{sub}}{(\sigma_B)_{main}} = \left(\frac{d_{sub}}{d_{main}}\right)^{-\frac{3}{m}}, \tag{16}$$

where $(\sigma_B)_{sub}$ and $(\sigma_B)_{main}$ are the breakage criteria of the sub and main particles, respectively. d_{sub} is the sub-particle diameter and d_{main} is the main grain's diameter. Moreover, Weibull's modulus is defined as m.

2.2.4. iDEM breakage algorithm

Our proposed algorithm can address all the discussed issues and model the dynamic breakage process by considering the natural morphology of the particle. The proposed method is summarized in Algorithm 1.

Algorithm 1. Breakage Algorithm Implemented in Image-based DEM

ALGORITHM 1: BREAKAGE ALGORITHM IMPLEMENTED IN IMAGE-BASED DEM

```
Input: Number of Particles (nParticle) and Overlaps
Output: Sub-grains distance fields and New nParticle

for i=0, nParticle do
    if particle(i) has contact with other particles and/or walls
        nodes forces to stress ← Eq. (10)
        Tresca and von Mises ← Eqs. (11) and (12)
        if σ_v > σ_B && σ_T > σ_B
            Finding contact forces
            Couple contact forces
            Calculate the stress field for each coupled force (Boussinesq)
            Reverse stress field
            Apply Dijkstra's algorithm
            Set operations
            26 Connected Component labeling
            sub-grains ← splitting original distance field
            Node-to-Surface ← Allocate nodes on the surface of new particles
            Properties of sub grains
            Designate to sub-particles ← Density, Velocity, and Force of the original particle to subs.
            nParticle ← nParticle + nSubParticles -1
        end if
    end if
end for
```

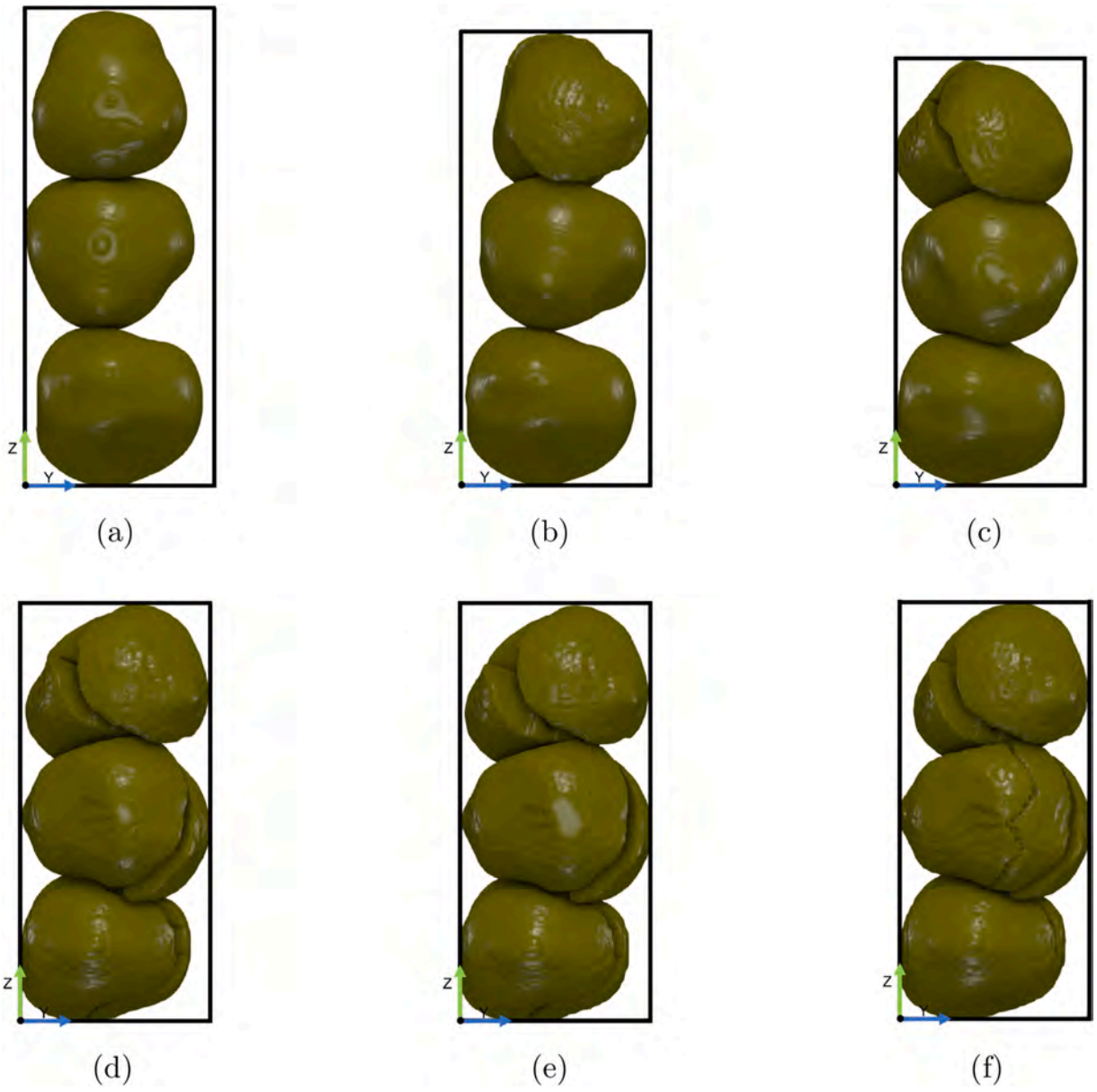

Fig. 13. Dynamic evolution of breakage process in the 2D YZ side view at time step (a) 0, (b) 100,000 (c) 170,000 (d) 199,000 (e) 200,000 and (f) 202,000.

3. Results and discussion

In this section, we discuss the results obtained from the proposed method. First, we will study the compression test on a spherical particle breakage to show the capability of our method visually as this problem has been studied widely, both experimentally and computationally. Table 1 summarizes the properties that have been used for this model based on previous studies.[23,29,50] Fig. 8 demonstrates the 3D breakage process of a spherical particle. As can be seen, fracture paths align with the fundamental understanding of fracture paths in a 1-D compression test, where the fractures are parallel to the loading direction.[51] To make a direct comparison between our results and those produced experimentally, one of such results is shown in Fig. 8(e), which demonstrates a reasonable reproduction of fracture paths. Moreover, to present our method's capabilities in capturing different breakage mechanisms, the top views of this simulation are shown in Fig. 9. In Fig. 9(b), the splitting mechanism is illustrated, which is followed by fragmentation and chipping in Fig. 9(c) and (d), respectively. Capturing such small chips shown in Fig. 9(d) can illustrate how such small features are reproduced. Furthermore, the top-view illustration reveals that the fractures concentrate close to the center of the spherical, which was expected.

After illustrating a single spherical grain breakage, the compression tests are conducted on a three-particle system, originally described in a previous experimental study by Cil and Alshibli.[23] In our simulations, we selected three particles with an average diameter of 0.75 mm to represent ASTM 20–30 Ottawa sand. The computational domain size was set to 1 mm × 1 mm × 2.5 mm. For the 1D compression test, the top wall of the domain was subjected to a constant displacement rate, the same as the experimental setup.[23] Fig. 10 illustrates the domain and particles at the beginning of the compression. In addition, Table 1 provides an overview of the properties used in our numerical investigation based on previous works.[23,29,50]

To validate our model, we have plotted the applied force from the top wall versus the vertical displacement in Fig. 11 and have compared it with previous experimental investigation[23] for breakage criteria set to

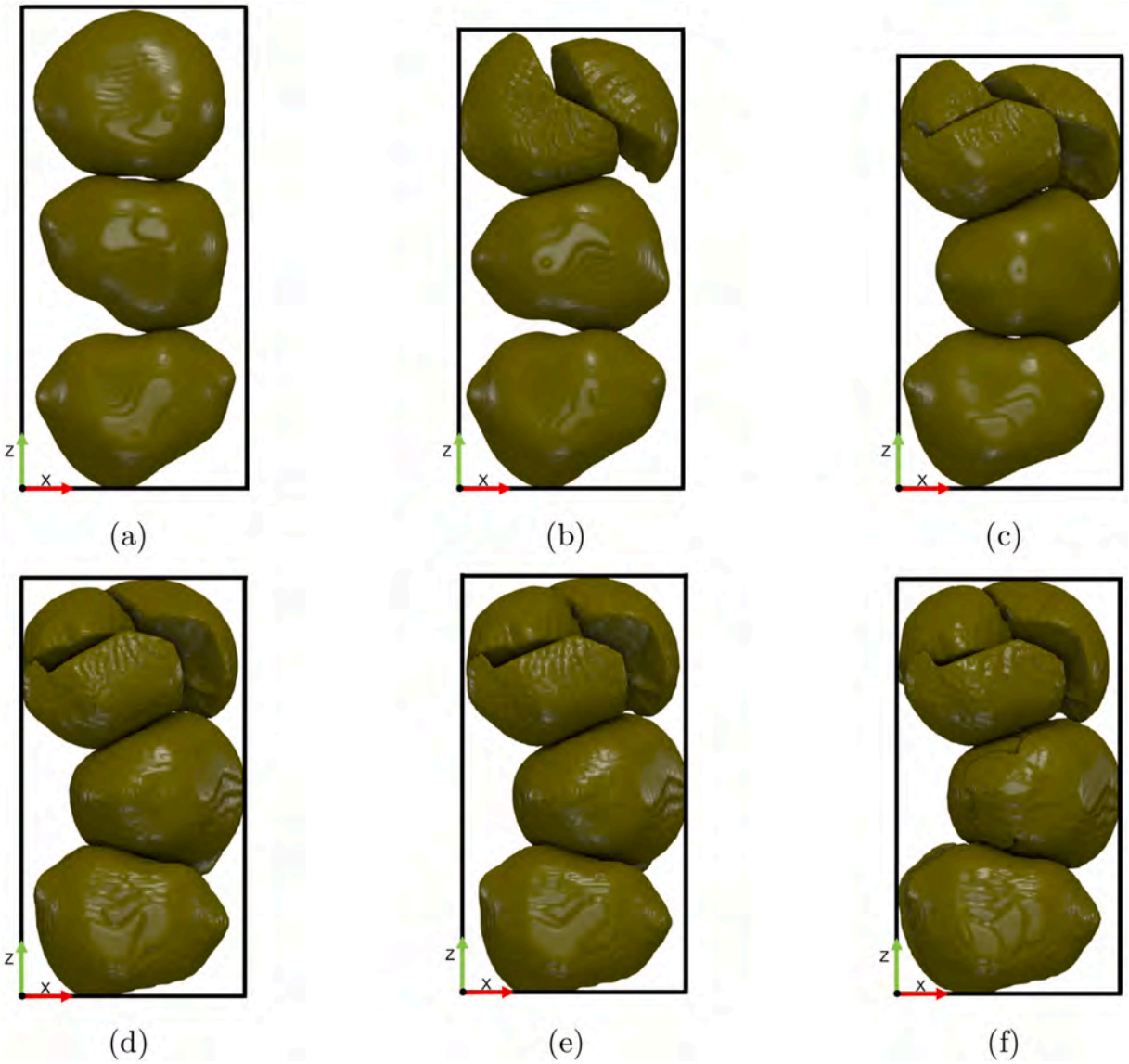

Fig. 14. Dynamic evolution of breakage process in the 2D XZ side view at time step (a) 0, (b) 100,000 (c) 170,000 (d) 199,000 (e) 200,000 and (f) 202,000.

45 MPa. Upon examining Fig. 11, we can observe an increasing trend in the applied load force until its peak (i.e., breaking point). However, after the breakage incident, the force load rapidly decreases. This behavior indicates that the force is applied to the particle until it breaks, and once breakage occurs, the force decreases as sub-grains find void spaces to move into. The trend of the calculated wall force aligns with the experimental data obtained by Cil and Alshibli,[23] despite the differences in particle morphology between our simulations and their experiments. We should note that the comparison was conducted until 0.2 mm of the vertical displacement since the experimental work was done until this displacement. However, we simulated our model until displacement of 0.4 mm to study the breakage comprehensively.

Fig. 12 provides a 3D illustration of the breakage evolution observed in the three-particle system during the compression test. The compression test can be divided into three distinct phases.

(I) In the initial phase, the particles attempt to find void spaces or rotate within the domain to avoid breakage. This phase is characterized by the particles' movements as they try to redistribute the applied forces.
(II) As the compression continues, if a particle is unable to find sufficient space for movement, either rotationally or translationally, it undergoes breakage. This phase is marked by the occurrence of particle fractures.
(III) After breakage, the applied force on the resulting sub-particles causes them to move into available void spaces within the domain until they become stuck again. This process of movement, breakage, and repositioning is repeated throughout the simulation.

For example, in Fig. 12(*a*), (*b*), and (*c*), the middle and bottom particles primarily experience phase (*I*), where they try to find room for movement. On the other hand, the top particle undergoes all three phases during these time steps. In contrast, in Fig. 12(*d*), (*e*), and (*f*), the top particle transfers the applied force from the wall to other grains, while the remaining particles go through all three phases to accommodate the compression force. In general, the breakage evolution observed in the simulation captures the dynamic response of the particles under compression and highlights the different phases involved in particle rearrangement and fracture.

To gain a better understanding of the breakage process and the different phases involved, it is beneficial to visualize the results in 2D from different viewing directions. Figs. 13 and 14 provide side views of the system in the YZ and XZ planes, respectively. Analyzing these figures

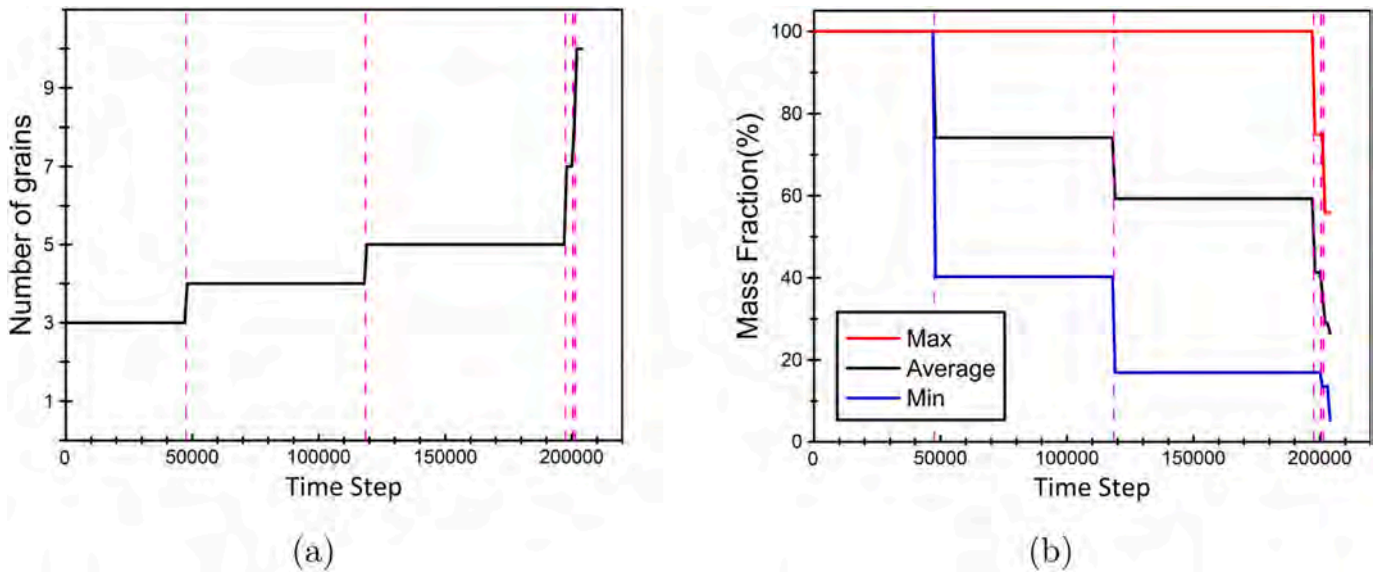

Fig. 15. Time evolution of (a) the number of grains and (b) the average, maximum, and minimum mass fraction in the domain during simulation.

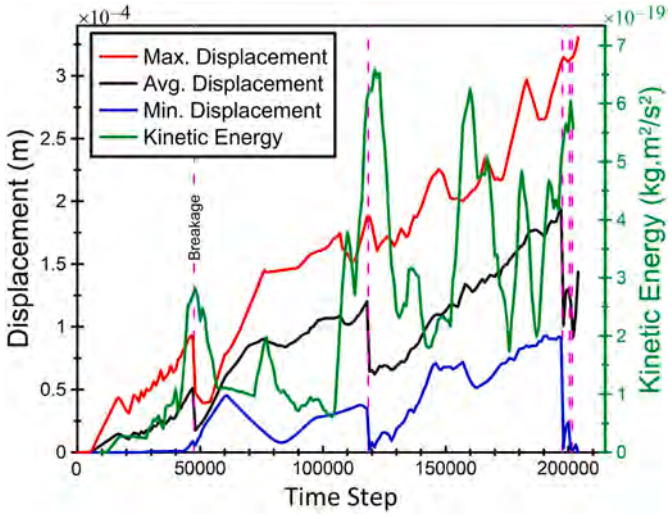

Fig. 16. Time evolution of the average displacement and kinetic energy of all grains in the computational domain.

reveals several interesting phenomena. In Fig. 13, a comparison between (a), (b), and (c) shows that the top particle, which experienced phases (*I*) and (*II*), undergoes another breakage in Fig. 13(b). This indicates the occurrence of multiple breakage events for the same particle. Additionally, comparing Fig. 13(b) and (c), one can observe rotational movements in the middle and bottom particles. These rotational motions play a crucial role in preventing these particles from breaking. Similar rotational movements around the Y-axis can also be observed in Fig. 14 (a), (b), and (c). Thus, the XZ side view (Fig. 14) reveals two distinct rotational patterns. The first pattern, observed in Fig. 14(a) and (b), involves rotation around the Y-axis and is primarily caused by the movement of the top particle. On the other hand, the comparison between Fig. 14(b), (c), and (d) reveals the second pattern, characterized by rotation around the Z-axis. This rotational motion is only observed in the middle particle and serves as an escape route for this particle to avoid breakage.

Quantifying these rotational motions is crucial, and this paper discusses the methods used to analyze and measure them. It should be noted that conventional DEM codes often lack the ability to accurately calculate such rotational movements due to their limited consideration of the natural shape of particles. In this paper, on the other hand, the 2D side view illustrations in Figs. 13 and 14 provide valuable insights into the breakage process and the occurrence of rotational movements, shedding light on the dynamic behavior of the particles during the compression test.

During our simulation, it is important to examine the number of grains in the domain to understand when breakage occurs over time. Fig. 15(a) presents the number of breakage incidents that occurred in the domain. As expected, in each breakage event, the number of grains increased. However, the particles break into more pieces as the domain becomes smaller due to the vertical displacement of the top wall. Initially, three particles were present, but at the end of the simulation, they broke and split into a total of 10 particles. Monitoring the mass of the particles in the system can also provide useful information in conjunction with the number of grains. Fig. 15(b) illustrates the minimum, maximum, and average mass fraction, which represents the ratio of the grain's mass to the original grain's mass ($=\frac{m_{grain}}{m_{original\ grain}}$). As depicted, by the end of the simulation, the average mass fraction has decreased by more than 70 %. This indicates that the particles have undergone significant breakage and fragmentation. As can be seen, the comparison between the force load and the number of grains provides insights into the occurrence of breakage incidents, and the analysis of the mass fraction reveals the extent of breakage and fragmentation that has taken place during the simulation.

The study of displacement can provide valuable insights into the relationship between breakage and particle movement. Fig. 16 illustrates the displacement versus time steps, along with the corresponding kinetic energy. It can be observed that during each breakage incident, the average displacement of particles decreases rapidly. However, after breakage, the trend reverses, and displacement increases again. This behavior is mirrored in kinetic energy as well. Our results indicate that breakage occurs when the displacement of a particle decreases, leading to a reduction in kinetic energy (i.e., energy release). In other words, during a compression test, if a particle fails to move or rotate due to a lack of void space, breakage is likely to occur. The observed fluctuations before and after breakage events support the discussion in this paper regarding the relationship between movement and breakage occurrence. Specifically, the newly formed fragments after breakage are smaller than the original particle and can easily occupy the available void spaces.

As mentioned earlier, we observed rotational motions in our simulations. To quantify these observations, we studied the pre-breakage

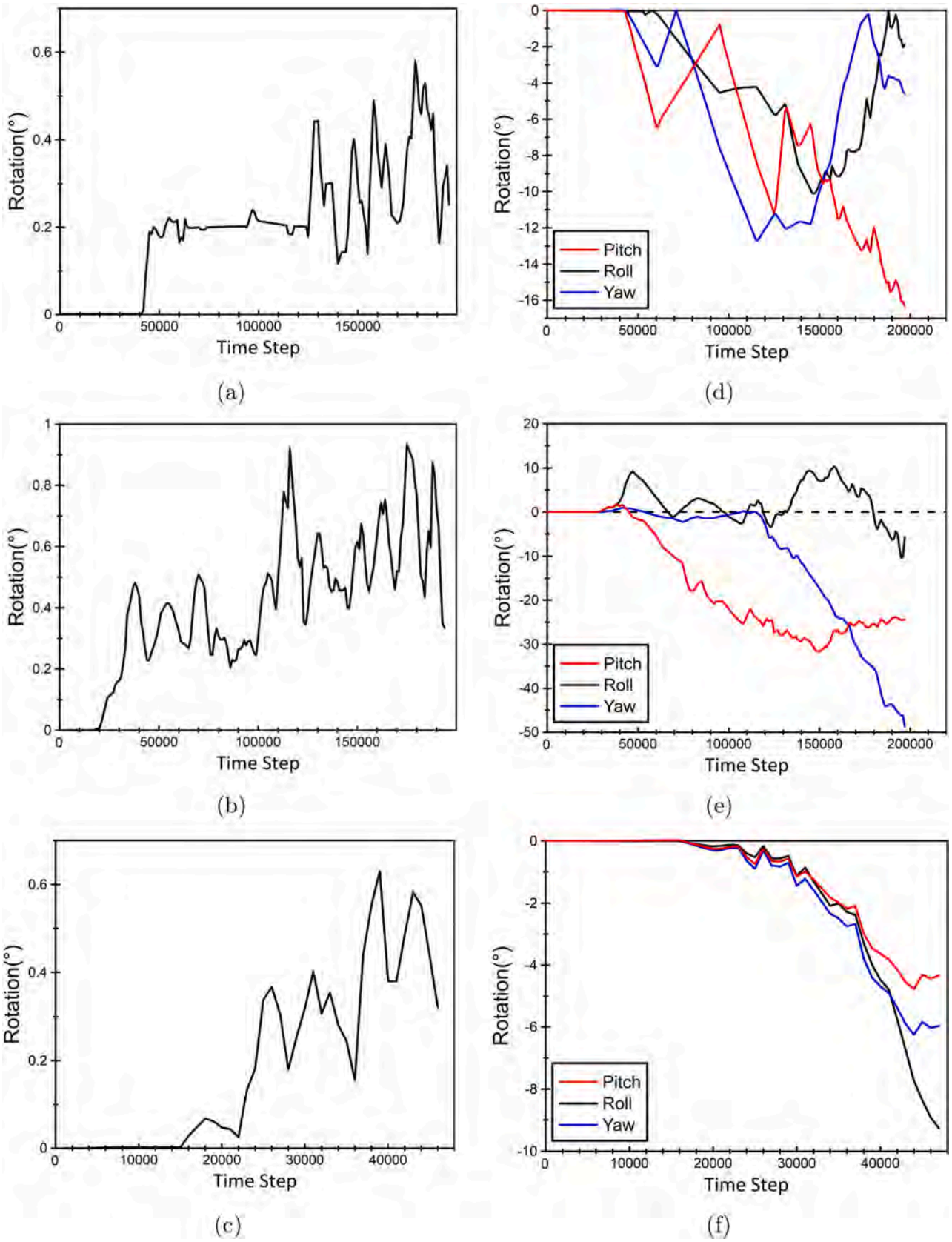

Fig. 17. Dynamic time evolution of pre-breakage average rotation in each time step of (a) the bottom, (b) the middle, and (c) the top particle and each direction rotation for (d) the bottom, (e) the middle, and (f) the top.

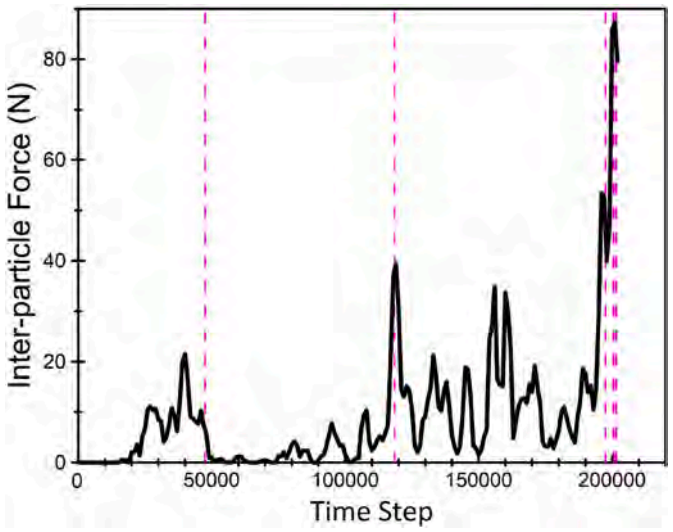

Fig. 18. Time evolution of the average particle-particle force for all grains during the simulation.

rotational behavior of each grain. Fig. 17(a) and (d) specifically focus on the bottom grain. In Fig. 17(a), the average Euler angles (i.e., roll, pitch, and yaw) for each time step are shown. The results indicate that the average rotation of the bottom grain does not exceed 0.6° at its highest. Fig. 17(d) provides a calculation of the rotational movement of the bottom grain from its original formation at the start of the simulation, considering each Euler rotation. It can be seen that the bottom particle has undergone a −16° pitch rolling displacement prior to its breakage. The highest rotational movements during the simulation are approximately −13° and −10° for yaw and roll, respectively. Therefore, the dominant rotational direction for this particle is pitch.

The rotational behavior of the middle particle before breakage is illustrated in Fig. 17(b) and (e). The average rotation in each time step reveals that, as observed in Figs. 13 and 14, the middle grain has experienced an average rotational motion of 1.8° during the breakage process. In contrast to the bottom particle - Fig. 17(a)- the middle particle exhibited two significant rotational patterns. Prior to its breakage, the middle particle rotated approximately 50° around its Y axis (yaw) and 25° in the pitch direction (Z axis), as shown in Fig. 17(e). Aside from these observations, after the breakage of the top particle (at time step ≈47,000), the average rotation increased due to the lateral movement of the top particle. This trend can be attributed to the release of energy observed in the system following breakage, as depicted in Fig. 17. Particularly, as shown in Fig. 11, the applied top-wall force reached its peak during each breakage incident. As explained earlier, grains are unable to find void spaces near each breakage event within the domain, leading them to experience rotational movement instead of lateral displacement.

The rotational behavior of the top particle prior to its breakage is depicted in Fig. 17(c) and (f). As shown, the average rotation of the top particle before breakage is not significantly high compared to the other grains, suggesting that its displacement can be primarily characterized as lateral movement. However, among the particles, the top particle exhibits a notable amount of rolling rotation just before its breakage. Therefore, at this stage, we have identified three distinct rotational behaviors among these particles. The top particle displays a dominant rolling rotation compared to yaw and pitch rotations observed in the middle grain and primarily pitch rotation in the bottom particle. While displacement remains a crucial parameter in understanding breakage, the influence of rotation should also be thoroughly studied in such systems. To achieve this, and as demonstrated in our results, it is crucial to consider the natural morphology of the grains in order to accurately capture these rotational motions.

The inter-particle force, which is a parameter that can influence breakage, is depicted in Fig. 18. It is observed that the inter-particle force increases before breakage occurs. However, the results indicate that the occurrence of breakage is not solely dependent on inter-particle forces. For instance, at time-step ∼ 40,000, the average inter-particle force reaches its highest value (prior to the first breakage), but none of the particles experience breakage. This can be attributed to displacement, as shown in Fig. 16. During this period of high force, the average displacement is still increasing, indicating that the force is causing particle movement rather than breakage. Furthermore, the first breakage event occurs in the top particle, which is in contact with the top wall. Therefore, in this initial breakage, the top particle fractures due to the strong force applied by the wall. However, the results indicate that particle-particle interactions contribute to the subsequent breakage

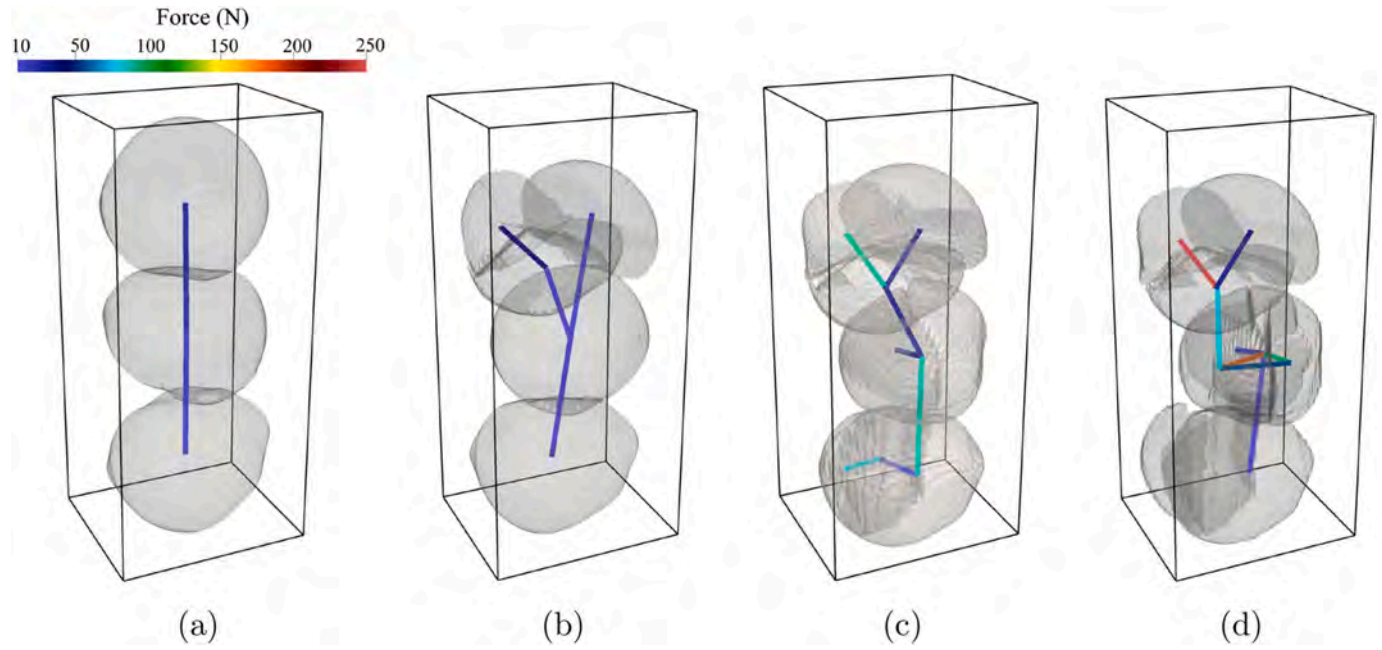

Fig. 19. Dynamic time evolution of force chain in the domain at time step (a) 33,000, (b) 159,000, (c) 200,000, and (d) 202,000.

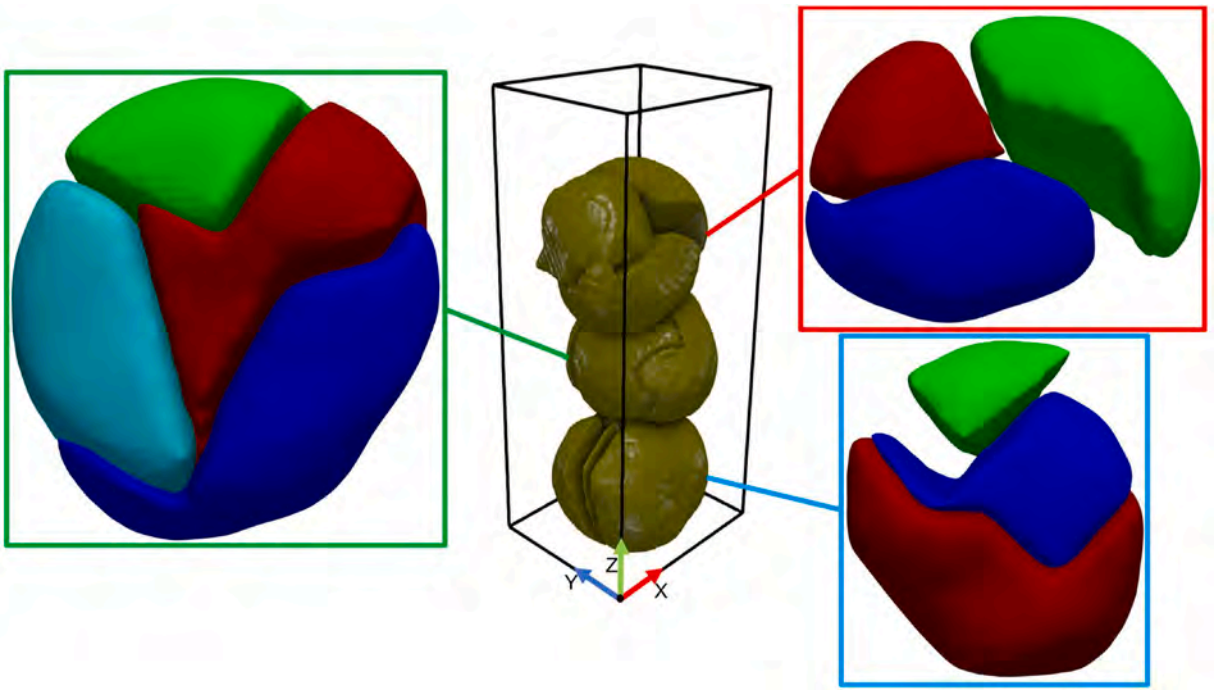

Fig. 20. Demonstration of sub-grains formation after going through the breakage process due to the compression test at the end of the simulation.

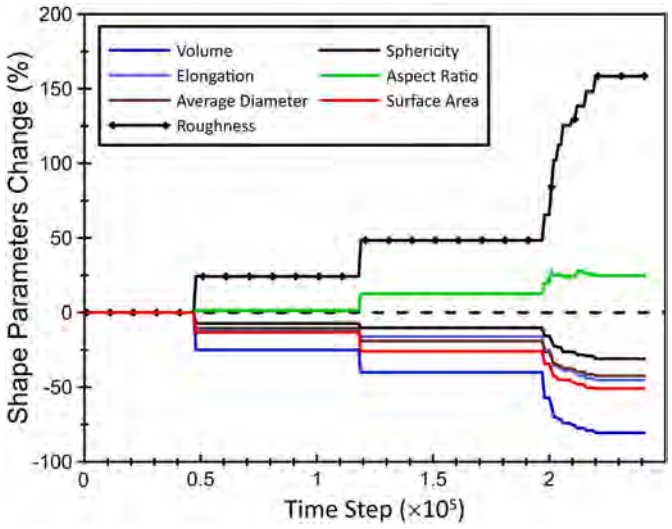

Fig. 21. Time evolution of the average shape parameters for all grains during the simulation.

incidents.

To enhance our understanding of inter-particle interactions, studying force chains provides valuable insights. Fig. 19 depicts the evolution of force chains at different time steps. Initially, vertical force transfer is evident before the occurrence of the first breakage event (Fig. 19 (a)). Subsequently, the force chains become more intricate after each breakage event. Notably, at the end of the simulation, a horizontal force chain between sub-particles emerges, which is not observed in the early stages (Fig. 19 (a) and (b)). Fig. 18 also demonstrates an increase in inter-particle force during the compression test, as mirrored in the force chain values. Consequently, breakage within the system impacts the magnitude and direction of force exchange between particles. During the compression test, there is a discernible force transition from the top to bottom particles due to the displacement of the top wall.

To illustrate the formation of sub-grains after the breakage process, Fig. 20 is presented. The irregular fracture paths and the particle fragmentation due to the breakage process can be seen in particles, which shows the capability of our method to capture the mentioned breakage characteristics. Fig. 20 depicts that grains tend to become more irregular at the end of breakage, which was expected.

To quantify our previous observations regarding the change in the shape of grains due to fracturing, we calculated various shape parameters over time. To this end, we demonstrated the time evolution of shape parameters during the simulation, which shows how the computed morphological parameters change during the simulation. In Fig. 21, the average roughness and aspect ratio of grains are the only shape parameters that experienced increasing trends during simulations. The reason can be found in the nature of breakage, which makes particles sharper as they experience fracturing. Hence, one should expect particles with more roughness and aspect ratio (i.e., irregularity). Furthermore, our results indicate that the average sphericity and volume of grains decreased by more than 30 % and 75 %, respectively, which is inline with our previous findings. The mentioned shape parameters are calculated using the following equations:

$$Elongation = \frac{Largest\ axis\ length}{Smallest\ axis\ length} \tag{17}$$

$$Roughness = \frac{Surface\ Area}{Volume} \tag{18}$$

$$Aspect\ Ratio = \frac{\text{Max}\ bounding\ box\ length}{\text{Min}\ bounding\ box\ lenght} \tag{19}$$

$$Sphericity = \frac{\sqrt[3]{36\pi Volume^2}}{Surface\ Area} \tag{20}$$

Here, we have changed the orientation of the previously studied pack to understand if the results are sensitive to the orientation and if they are, then, how variable the result might be. As shown in Fig. 22(a–c), we changed the initial orientation of grains systematically, and results for each case are demonstrated in Fig. 22(*d*–f), respectively. One can clearly observe the different behavior of these setups at the end of simulations.

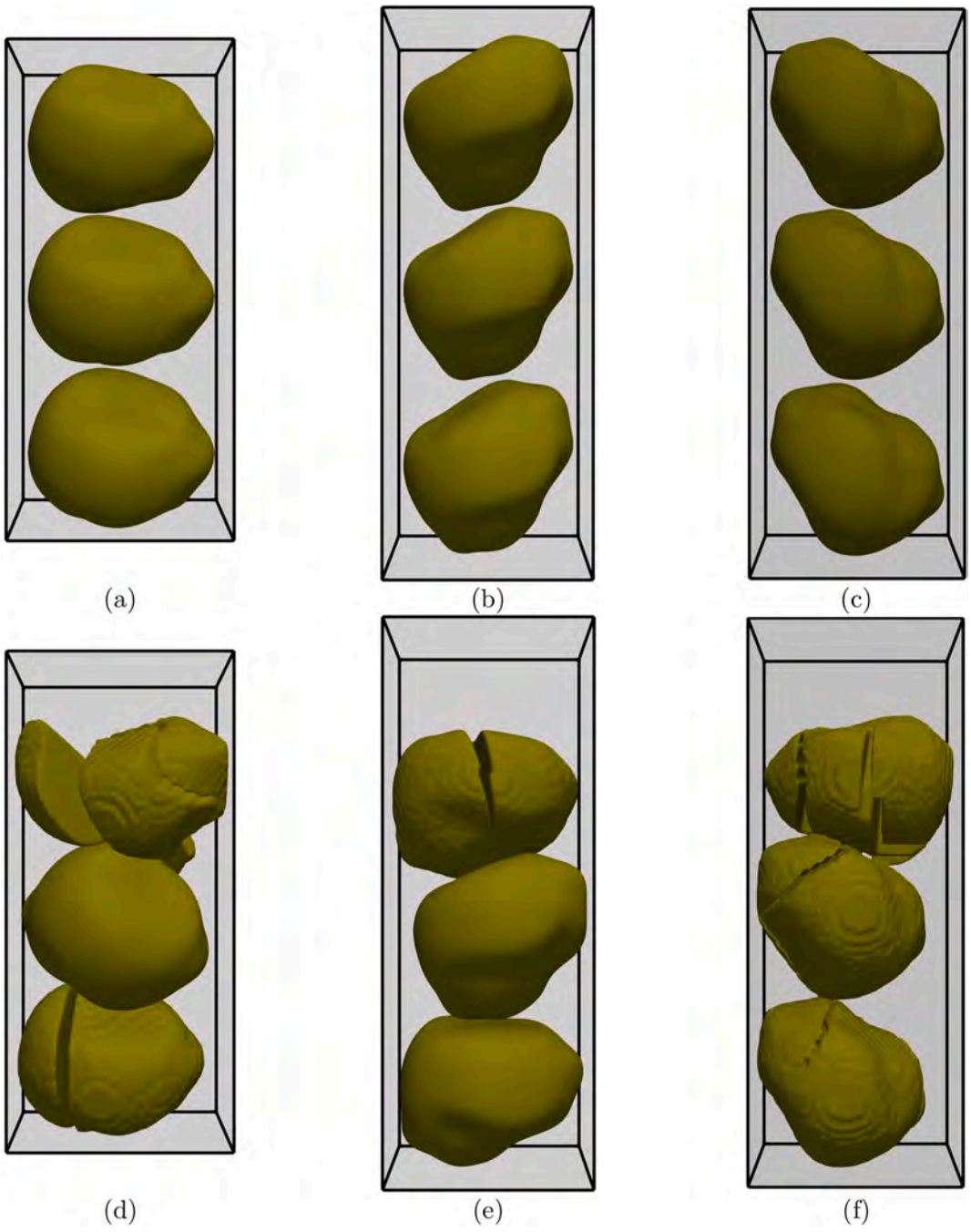

Fig. 22. Demonstration of three particle systems under 1-D compression at the initial time-step (upper row) and at the end of simulations (lower row).

As can be seen in Fig. 22 (d), at the first setup (i.e., Fig. 22 (a)), the middle particle remained unbroken. For the second orientation (i.e., Fig. 22 (b) and (e)), the top particle only experienced damage. On the other hand, all grains went through the breakage in the third setup; see Fig. 22 (c) and (f). The comparison in this figure reveals that the initial orientation of particles can play an essential role in defining the occurrence of breakage and fracture paths.

To quantify our observations regarding the influence of the initial orientation of grains, different shape parameters have been studied. To this end, we illustrated a wide range of shape characteristics in Fig. 23. The error bars in Fig. 23 represent the standard error of the Probability Density Function at each corresponding shape parameter. Both bimodal (Fig. 23 (a) and (d)) and multimodal (e.g., volume) distributions can be seen in Fig. 23, which can be interpreted into multiple subpopulations of the data. Thus, it showed that particles in different orientation setup have different morphological properties. The different distribution pattern for shape parameters illustrated that one can expect a wide range of shape parameters values in such simulations. Furthermore, as can be seen in Fig. 23 (a), the Aspect Ratio has the highest variation among shape parameters which indicates a higher variability in the estimated PDF. To sum up, our results highlight the importance of initial orientation since it can change the fracture paths, which leads to a change in the shape of grains.

4. Summary and conclusions

The breakage process is relevant in various applications, and accurately modeling such systems poses a challenge. While considering the

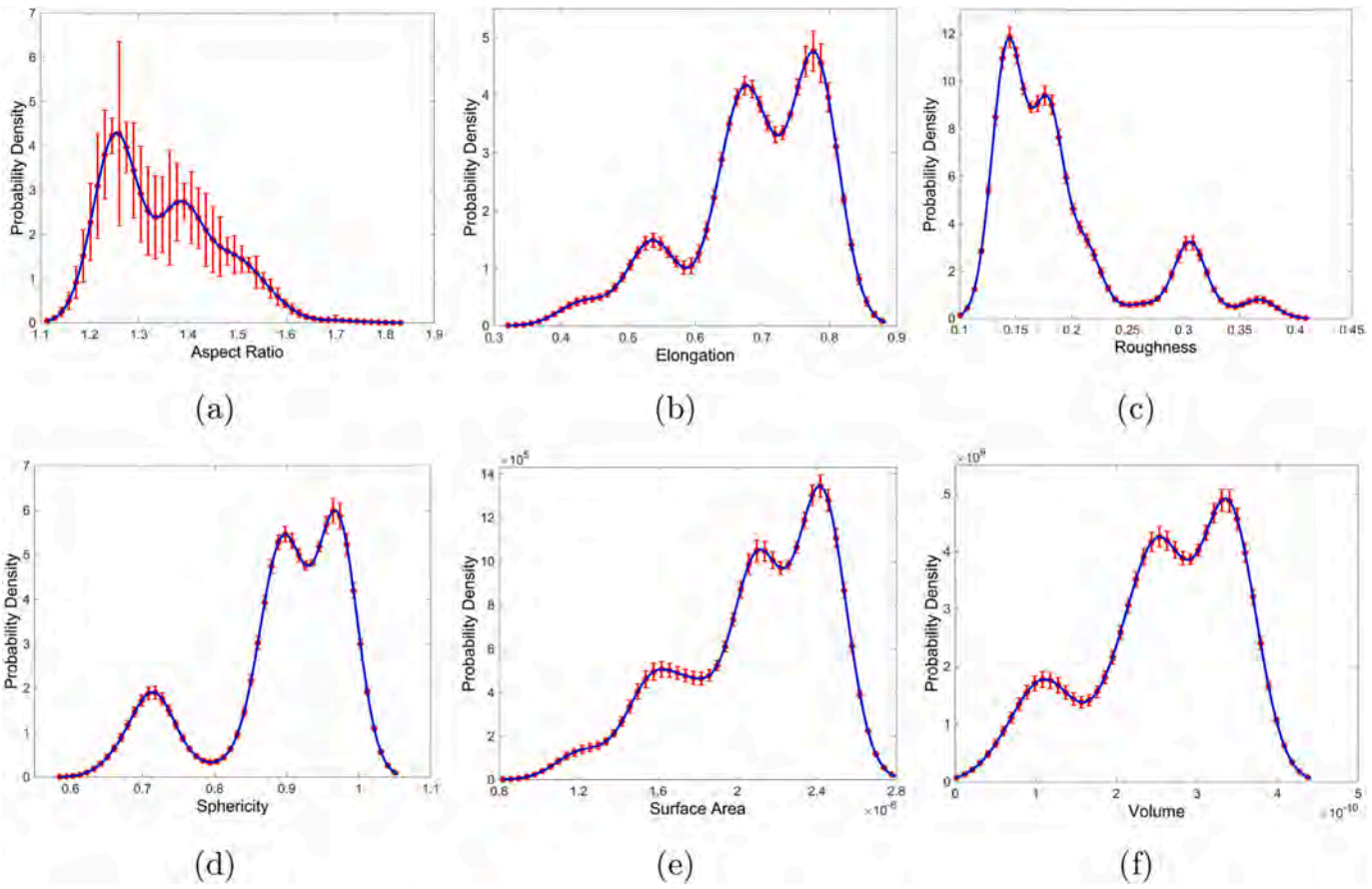

Fig. 23. Probability Density Function (PDF) with respect to (a) Aspect Ratio, (b) Elongation, (c) Roughness, (d) Sphericity, (e) Surface Area, and (f) Volume for all initial orientations' simulations.

actual morphology of particles can lead to more realistic results, it also adds complexity to the model. Previous numerical studies have not incorporated fragmentation breakage scenarios (involving multiple fracture surfaces) and non-planar fracture surfaces, mainly due to simplification concerns. In this study, we introduced an innovative method that addresses these limitations by incorporating irregular particle morphology, multiple fracture surfaces, and non-planar fracture surfaces. To achieve this, we have enhanced the image-based Discrete Element Method (iDEM) by integrating it with a graph-based method for fracture surface identification. Additionally, we have utilized 26 connected components labeling and set operations to create sub-grains, enabling a more comprehensive representation of the breakage process.

To investigate the proposed breakage model, we applied the method to a compression test on a three-particle system and compared the results with experimental data. Our aim was to gain a comprehensive understanding of the behavior of particles before and after breakage. During the simulations, we analyzed various parameters, including the number of grains, mass fraction, displacement, kinetic energy, rotational motions, and inter-particle force. Through this numerical investigation, we obtained intriguing findings that shed light on the breakage process and its associated phenomena, which are.

I. At the end of the simulation, all original particles broke, and the number of grains reached 10.
II. The smallest grain's mass is one-tenth of the original grain (i.e., unbroken), and the average mass of the system decreased by 80 %.
III. Before each breakage event, the displacement of particles increased, and during breakage, a rapid decline was observed.
IV. The energy release after each breakage incident was also observed in our results.
V. The rotational motion of a particle should not be neglected in such a system. Although the top wall moves laterally, each particle has its own rotational motion. Among particles, the middle particle, since its motion is not limited to the top or bottom wall, has the most rotational motion.
VI. The inter-particle can cause the breakage, although, at the first breakage event, the top wall-particle interaction is the reason for the breakage.
VII. The change in initial orientations of particles can lead to different fracture paths, which means a change in grains' shape.

Therefore, conducting a thorough investigation of irregular particle breakage while considering multiple non-planar fracture surfaces can provide valuable insights. The proposed method allows for the identification of microscale characteristics of grains before and after each breakage event. In future studies, this method can be applied to various breakage applications across different scales, further enhancing our understanding of the breakage process. Moreover, alternative criteria can be formulated to delineate fracture paths and fragmentations. In this study, our primary focus lies in delineating an irregular fracture path within a stress field. One approach involves utilizing a combination of stress and other fracture criteria, generating a scalar map within each particle. This map serves as a foundation for producing a more realistic field, integral to the fracture path identification algorithm discussed in this paper.

CRediT authorship contribution statement

Mehryar Amir Hosseini: Methodology, Formal analysis, Investigation, Software, Validation, Visualization, Writing – original draft. **Pejman Tahmasebi:** Conceptualization, Formal analysis, Funding acquisition, Methodology, Supervision, Writing – review & editing.

Declaration of competing interest

The authors declare that they have no known competing financial interests or personal relationships that could have appeared to influence the work reported in this paper.

Data availability

Data will be made available on request.

Acknowledgments

The authors would like to thank the financial support from the Colorado School of Mines for this research.

References

1. Wu Z, Zhang P, Fan L, Liu Q. Numerical study of the effect of confining pressure on the rock breakage efficiency and fragment size distribution of a TBM cutter using a coupled FEM-DEM method. *Tunn Undergr Space Technol*. 2019;88:260–275. https://doi.org/10.1016/j.tust.2019.03.012.
2. Li HY, Chai HW, Xiao XH, Huang JY, Luo SN. Fractal breakage of porous carbonate sand particles: microstructures and mechanisms. *Powder Technol*. 2020;363:112–121. https://doi.org/10.1016/J.POWTEC.2020.01.007.
3. Picart L, Mazel V, Moulin A, Bourgeaux V, Tchoreloff P. Breaking patterns of press-coated tablets during the diametral compression test: influence of the product, geometry and process parameters. *Int J Pharm*. 2022;612, 121371. https://doi.org/10.1016/J.IJPHARM.2021.121371.
4. Xiao P, Guo Y, Wang J, et al. The effect of granules characters on mechanical properties of press-coated tablets: a comparative study. *Int J Pharm*. 2022;624, 121986. https://doi.org/10.1016/J.IJPHARM.2022.121986.
5. Shen J, Chen X, Wang Xing, Wang Xinzhi, Qin Y, Wu H. Compression responses and particle breakage of calcareous granular material in reclaimed islands. *Powder Technol*. 2023, 118277. https://doi.org/10.1016/J.POWTEC.2023.118277.
6. Sapozhnikov OA, Maxwell AD, MacConaghy B, Bailey MR. A mechanistic analysis of stone fracture in lithotripsy. *J Acoust Soc Am*. 2007;121:1190. https://doi.org/10.1121/1.2404894.
7. Ma G, Zhou W, Regueiro RA, Wang Q, Chang X. Modeling the fragmentation of rock grains using computed tomography and combined FDEM. *Powder Technol*. 2017;308:388–397. https://doi.org/10.1016/J.POWTEC.2016.11.046.
8. Cavarretta I, O'Sullivan C. The mechanics of rigid irregular particles subject to uniaxial compression. *Geotechnique*. 2012;62:681–692. https://doi.org/10.1680/GEOT.10.P.102/ASSET/IMAGES/SMALL/GEOT62-0681-F14.GIF.
9. Kandasami RK, Murthy TG. Manifestation of particle morphology on the mechanical behaviour of granular ensembles. *Granul Matter*. 2017;19:1–13. https://doi.org/10.1007/S10035-017-0703-Z/FIGURES/9.
10. Peña AA, García-Rojo R, Herrmann HJ. Influence of particle shape on sheared dense granular media. *Granul Matter*. 2007;9:279–291. https://doi.org/10.1007/s10035-007-0038-2.
11. Wang W, Coop MR. An investigation of breakage behaviour of single sand particles using a high-speed microscope camera. *Geotechnique*. 2016;66:984–998. https://doi.org/10.1680/JGEOT.15.P.247/ASSET/IMAGES/SMALL/JGEOT.15.P.247-F30.GIF.
12. Cundall PA, Strack ODL. A discrete numerical model for granular assemblies. *Geotechnique*. 1979;29:47–65. https://doi.org/10.1680/geot.1979.29.1.47.
13. Chen L, Jin A, Wu S, Chu C, Li X. Numerical study on spalling failure of rock surrounding deep buried tunnel based on DEM. *Comput Geotech*. 2022;145. https://doi.org/10.1016/J.COMPGEO.2022.104653.
14. Cun Z, Bo L, Ziyu S, Jinbao L, Jinlong Z. Breakage mechanism and pore evolution characteristics of gangue materials under compression. *Acta Geotech*. 2022;17:4823–4835.
15. Potyondy DODDO, Cundall PAPA. A bonded-particle model for rock. *Int J Rock Mech Min Sci*. 2004;41:1329–1364. https://doi.org/10.1016/J.IJRMMS.2004.09.011.
16. Su Y, Xu Y, Cui T, et al. A combined experimental and DEM approach to optimize the centrifugal maize breakage tester. *Powder Technol*. 2022;397. https://doi.org/10.1016/J.POWTEC.2021.11.052.
17. Tomac I, Gutierrez M. Coupled hydro-thermo-mechanical modeling of hydraulic fracturing in quasi-brittle rocks using BPM-DEM. *J Rock Mech Geotech Eng*. 2017;9:92–104. https://doi.org/10.1016/J.JRMGE.2016.10.001.
18. Cao R hong, Yao R, Lin H, Lin Q bin, Meng Q, Li T. Shear behaviour of 3D nonpersistent jointed rock-like specimens: experiment and numerical simulation. *Comput Geotech*. 2022;148, 104858. https://doi.org/10.1016/J.COMPGEO.2022.104858.
19. Chen X, Peng D, Morrissey JP, Ooi JY. A comparative assessment and unification of bond models in DEM simulations. *Granul Matter*. 2022;24:29. https://doi.org/10.1007/s10035-021-01187-2.
20. Li K, Cheng Y, Fan X. Roles of model size and particle size distribution on macro-mechanical properties of Lac du Bonnet granite using flat-joint model. *Comput Geotech*. 2018;103:43–60. https://doi.org/10.1016/J.COMPGEO.2018.07.007.
21. Wu S, Xu X. A study of three intrinsic problems of the classic discrete element method using flat-joint model. *Rock Mech Rock Eng*. 2016;49:1813–1830. https://doi.org/10.1007/S00603-015-0890-Z/FIGURES/23.
22. Zhang X, Tahmasebi P. Coupling irregular particles and fluid: complex dynamics of granular flows. *Comput Geotech*. 2022;143, 104624. https://doi.org/10.1016/j.compgeo.2021.104624.
23. Cil MB, Alshibli KA. *3D Assessment of Fracture of Sand Particles Using Discrete Element Method 2*. 2012:161–166.
24. Åström JA, Herrmann HJ. Fragmentation of grains in a two-dimensional packing. *Eur Phys J B*. 1998;5:551–554. https://doi.org/10.1007/S100510050476/METRICS.
25. Ben-Nun O, Einav I. The role of self-organization during confined comminution of granular materials. *Philos. Trans. R. Soc. A Math. Phys. Eng. Sci.* 2010;368:231–247.
26. Cil MB, Buscarnera G. DEM assessment of scaling laws capturing the grain size dependence of yielding in granular soils. *Granul Matter*. 2016;18:36. https://doi.org/10.1007/s10035-016-0638-9.
27. McDowell GR, de Bono JP. On the micro mechanics of one-dimensional normal compression. *Geotechnique*. 2013;63:895–908. https://doi.org/10.1680/geot.12.P.041.
28. Zhou W, Xu K, Ma G, Chang X. On the breakage function for constructing the fragment replacement modes. *Particuology*. 2019;44:207–217. https://doi.org/10.1016/J.PARTIC.2018.08.006.
29. Harmon JM, Arthur D, Andrade JE. Level set splitting in DEM for modeling breakage mechanics. *Comput Methods Appl Mech Eng*. 2020;365, 112961. https://doi.org/10.1016/J.CMA.2020.112961.
30. Pazmiño SA, Jerves AX, Dijkstra J, Medina DA, Jostad HP. A generalized 3DLS-DEM scheme for grain breakage. *Comput Methods Appl Mech Eng*. 2022;399, 115383. https://doi.org/10.1016/J.CMA.2022.115383.
31. Desrues J, Viggiani G, Bésuelle P. *Advances in X-ray tomography for geomaterials*. In: *Advances in X-Ray Tomography for Geomaterials*. Wiley-ISTE; 2010. https://doi.org/10.1002/9780470612187.
32. Houlsby GTT. Potential particles: a method for modelling non-circular particles in DEM. *Comput Geotech*. 2009;36:953–959. https://doi.org/10.1016/j.compgeo.2009.03.001.
33. Zhang X, Tahmasebi P. Investigation of particle shape and ambient fluid on sandpiles using a coupled micro-geomechanical model. *Powder Technol*. 2022, 117711. https://doi.org/10.1016/j.powtec.2022.117711.
34. Jiang Y, Mora P, Herrmann HJ, Alonso-Marroquín F. Damage separation model: a replaceable particle method based on strain energy field. *Phys Rev E*. 2021;104, 45311. https://doi.org/10.1103/PhysRevE.104.045311.
35. Zhang X, Tahmasebi P. Drafting, kissing and tumbling process of two particles: the effect of morphology. *Int J Multiphas Flow*. 2023;160, 104379. https://doi.org/10.1016/J.IJMULTIPHASEFLOW.2023.104379.
36. Bailey DG. An efficient euclidean distance Transform. *Lect Notes Comput Sci*. 2004;3322:394–408. https://doi.org/10.1007/978-3-540-30503-3_28.
37. Hosseini MA, Tahmasebi P. On the influence of the natural shape of particles in multiphase fluid systems: granular collapses. *Comput Geotech*. 2023;162, 105654. https://doi.org/10.1016/J.COMPGEO.2023.105654.
38. Lim K-W, Andrade JE. Granular element method for three-dimensional discrete element calculations. *Int J Numer Anal Methods GeoMech*. 2014;38:167–188. https://doi.org/10.1002/nag.2203.
39. Jiang Y, Herrmann HJ, Alonso-Marroquin F. A boundary-spheropolygon element method for modelling sub-particle stress and particle breakage. *Comput Geotech*. 2019;113. https://doi.org/10.1016/j.compgeo.2019.05.002.
40. Ramesh K, Shins K. Stress field equations for a disk subjected to self-equilibrated arbitrary loads: revisited. *Granul Matter*. 2022;24:49. https://doi.org/10.1007/s10035-021-01205-3.
41. Al-Derbi MS, De Freitas MH. Use of the boussinesq equation for determining the distribution of stress within a diametrical point load test. *Rock Mech Rock Eng*. 1999;32:257–265. https://doi.org/10.1007/S006030050047/METRICS.
42. Estay DA, Chiang LE. Discrete crack model for simulating rock comminution processes with the Discrete Element Method. *Int J Rock Mech Min Sci*. 2013;60:125–133. https://doi.org/10.1016/J.IJRMMS.2012.12.041.
43. Forbes M, Masoumi H, Saydam S, Hagan P. *Investigation into the Effect of Length to Diameter Ratio on the Point Load Strength Index of Gosford Sandstone*. 2015.
44. Hurley RC, Lind J, Pagan DC, Akin MC, Herbold EB. In situ grain fracture mechanics during uniaxial compaction of granular solids. *J Mech Phys Solid*. 2018;112:273–290. https://doi.org/10.1016/J.JMPS.2017.12.007.
45. Barbehenn M. A note on the complexity of Dijkstra's algorithm for graphs with weighted vertices. *IEEE Trans Comput*. 1998;47:263. https://doi.org/10.1109/12.663776.
46. Dijkstra EW. A note on two problems in connexion with graphs. *Numer Math*. 1959;1:269–271. https://doi.org/10.1007/BF01386390/METRICS.
47. Javaid MA. *Understanding Dijkstra's Algorithm*. SSRN Electron. J; 2013. https://doi.org/10.2139/SSRN.2340905.
48. Mahmud K, Mariethoz G, Caers J, Tahmasebi P, Baker A. Simulation of Earth textures by conditional image quilting. *Water Resour Res*. 2014;50:3088–3107. https://doi.org/10.1002/2013WR015069.

49. Nakata Y, Hyde AFL, Hyodo M, Murata H. *A Probabilistic Approach to Sand Particle Crushing in the Triaxial Test*. 2015:567–583. https://doi.org/10.1680/GEOT.1999.49.5.567.
50. Harmon JM, Seo D, Buscarnera G, Andrade JE. *Insight into Contact Forces in Crushable Sand Using Experiments and Predictive Particle-Scale Modeling*. GIF; 2022. https://doi.org/10.1680/JGEOT.21.00212/ASSET/IMAGES/SMALL/JGEOT.21.00212-F13. Geotechnique.
51. Li YW, Zhang J, Liu Y. Effects of loading direction on failure load test results for Brazilian tests on coal rock. *Rock Mech Rock Eng*. 2016;49:2173–2180. https://doi.org/10.1007/S00603-015-0841-8/FIGURES/9.